Atmos. Chem. Phys. Discuss., 13, 26529–26578, 2013
www.atmos-chem-phys-discuss.net/13/26529/2013/
doi:10.5194/acpd-13-26529-2013

Atmospheric Chemistry and Physics Discussions
Open Access

Atmospheric inversion of the surface CO_2 flux with $^{13}CO_2$ constraint

J. M. Chen[1,2], G. Mo[1], and F. Deng[1]

[1]Department of Geography and Program in Planning, University of Toronto, 100 St. George Street, Toronto, Ontario, M5S 3G3, Canada
[2]International Institute of Earth System Science, Nanjing University, 22 Hankou Road, Nanjing, Jiangsu, 210093, China

Received: 12 September 2013 – Accepted: 17 September 2013 – Published: 14 October 2013

Correspondence to: J. M. Chen (chenj@geog.utoronto.ca)

Published by Copernicus Publications on behalf of the European Geosciences Union.

Abstract

Observations of $^{13}CO_2$ at 73 sites compiled in the GLOBALVIEW database are used for an additional constraint in a global atmospheric inversion of the surface CO_2 flux using CO_2 observations at 210 sites for the 2002–2004 period for 39 land regions and 11 ocean regions. This constraint is implemented using the $^{13}CO_2/CO_2$ flux ratio modeled with a terrestrial ecosystem model and an ocean model. These models simulate $^{13}CO_2$ discrimination rates of terrestrial photosynthesis and respiration and ocean-atmosphere diffusion processes. In both models, the $^{13}CO_2$ disequilibrium between fluxes to and from the atmosphere is considered due to the historical change in atmospheric $^{13}CO_2$ concentration. For the 2002–2004 period, the $^{13}CO_2$ constraint on the inversion increases the total land carbon sink from 3.40 to 3.70 $\mathrm{Pg\,C\,yr^{-1}}$ and decreases the total oceanic carbon sink from 1.48 to 1.12 $\mathrm{Pg\,C\,yr^{-1}}$. The largest changes occur in tropical areas: a considerable decrease in the carbon source in the Amazon forest, and this decrease is mostly compensated by increases in the ocean region immediately west of the Amazon and the southeast Asian land region. Our further investigation through different treatments of the $^{13}CO_2/CO_2$ flux ratio used in the inversion suggests that variable spatial distributions of the $^{13}CO_2$ isotopic discrimination rate simulated by the models over land and ocean have considerable impacts on the spatial distribution of the inverted CO_2 flux over land and the inversion results are not sensitive to errors in the estimated disequilibria over land and ocean.

1 Introduction

Over the last few decades, much progress has been made in estimating the global carbon cycle using different methods (Houghton et al., 2007; Canadell et al., 2007; Le Quéré et al., 2009). In particular, atmospheric CO_2 data measured near the surface have been used to infer the carbon flux over land and ocean surfaces through atmospheric inversion (Rödenbeck et al., 2003; Michalak et al., 2005; Peylin et al., 2005;

ACPD
13, 26529–26578, 2013

Peters et al., 2007). However, the uncertainty in the inferred flux is still very large, mostly because of the insufficient number of observation stations and the error in modeling the atmospheric transport of CO_2 from the surface to the observation stations. To reduce this uncertainty, it would be useful to introduce constraints to the inversion using other gas species that are associated the CO_2 flux.

Measurements of the atmospheric concentration of the stable isotope $^{13}CO_2$ at a number of stations across the globe since 1994 have been compiled in a database (GLOBALVIEW-CO2C13, 2009), and the number increased to 76 by 2009. The mole fraction of $^{13}CO_2$ to CO_2 in the atmosphere is about 1.1 %, and the CO_2 exchange between the surface and the atmosphere would inevitably involve $^{13}CO_2$ exchange. However, the proportion of the $^{13}CO_2$ flux relative to the CO_2 flux differs at different locations and different times due to different mechanisms that discriminate against the heavier $^{13}CO_2$ molecules in the exchange processes, and therefore the $^{13}CO_2$ concentration measured in the atmosphere contains additional information for the CO_2 flux. This information is useful for differentiating between terrestrial and oceanic CO_2 exchanges with the atmosphere because the terrestrial CO_2 flux experiences much greater discrimination against $^{13}CO_2$ than does the oceanic CO_2 flux (Tans et al., 1990; Ciais et al., 1995b; Francey et al., 1995). The other potential use of $^{13}CO_2$ data is to differentiate between photosynthetic and respiratory fluxes over land as these two fluxes have different rates of discrimination against $^{13}CO_2$ (Fung et al., 1997; Randerson et al., 2002; Suits et al., 2005). The $^{13}CO_2$ observations over the globe, albeit with a limited number of stations, could therefore be used to assist in quantifying the global carbon cycle.

In previous studies (Siegenthaler and Oeschger, 1987; Keeling et al., 1989a; Francey et al., 1995; Randerson et al., 2002), atmospheric $^{13}CO_2$ observations have been used to separate ocean and land CO_2 fluxes through the use of a technique dubbed "double deconvolution", by which the CO_2 fluxes of land and ocean are separated (deconvolved) based on different discrimination rates against $^{13}CO_2$ in the atmospheric CO_2 exchange with land and ocean surfaces. This double deconvolution necessarily assumes that the discrimination rates over land and ocean are uniform and constant.

ACPD
13, 26529–26578, 2013

Through forward atmospheric transport modeling, the ocean and land CO_2 fluxes were also separated based on the spatial gradients of the measured $^{13}CO_2/CO_2$ ratio either globally (Keeling et al., 1989b) or by latitudinal bands (Ciais et al., 1995a). The same $^{13}CO_2$ data have also been used in inverse modeling of the surface CO_2 flux (Enting et al., 1995; Rayner et al., 1999, 2008). Enting et al. (1995) pioneered a methodology for inverting annual mean ocean and land CO_2 fluxes from both atmospheric CO_2 and $^{13}CO_2$ concentration data for 12 ocean regions and 8 land ecosystems for the 1986–1987 and 1989–1990 periods. Rayner et al. (1999) developed a different methodology to invert monthly CO_2 fluxes for 12 ocean and 14 land regions for the period from 1980 to 1995 from CO_2 observations at 12 stations and $^{13}CO_2$ and O_2/N_2 observations at 1 station. Rayner et al. (2008) refined their methodology and applied it to the period from 1992 to 2005 using CO_2 at from 67 sites and $^{13}CO_2$ at 10 sites. These studies showed the usefulness of the additional information from $^{13}CO_2$ observations in improving the inversion of annual mean and seasonality of the CO_2 flux over land and ocean. In these inversion studies, the discrimination rate for land is either assumed to be a constant (Enting et al., 1995; Rayner et al., 1999) or allowed to vary with the areal fraction of C4 plant in a region (Rayner et al., 2008). These inversions based on the Bayesian principle were also constrained with only simple prior estimates of the terrestrial and oceanic CO_2 and $^{13}CO_2$ fluxes. Since the data density (the numbers of CO_2 and $^{13}CO_2$ observation sites) is low, the assumed discrimination constants and these prior estimates would have considerable influence on the inverted results, as this is clearly demonstrated in Enting et al. (1995).

The overall goal of this study is to explore the information content of $^{13}CO_2$ measurements for global CO_2 flux estimation through developing a Bayesian synthesis inversion system that uses both CO_2 and $^{13}CO_2$ observations. This system is used to address the following specific objectives: (1) to investigate the difference in the inverted CO_2 flux by including $^{13}CO_2$ data in the inversion, (2) to evaluate the importance of considering the spatial distributions of the $^{13}CO_2$ discrimination rate over land and ocean in

ACPD
13, 26529–26578, 2013

the inversion of the CO_2 flux, and (3) to assess the impacts of $^{13}CO_2$ disequilibria over land and ocean on the CO_2 inversion results. To achieve these objectives, a terrestrial ecosystem model named the Boreal Ecosystem Productivity Simulator (BEPS) is further developed to simulate the spatial distributions of the $^{13}CO_2$ discrimination and disequilibrium rates over land and used them in a global synthesis Bayesian inversion with $^{13}CO_2$ constraint. BEPS is also used to produce CO_2 and $^{13}CO_2$ fluxes globally as prior fluxes to regularize the inversion.

2 Methodology

2.1 The inversion method

2.1.1 Inversion system

The nested inversion system with a focus on North America developed by Deng et al. (2007) is adopted in this study. In this system, two of the Transcom regions (Gurney et al., 2002) in North America are divided into 30 regions according to ecosystem type and administrative boundaries (Fig. 1), in order to reduce spatial aggregation errors in the inversion over North America and to investigate the inverted spatial distribution of the carbon flux against ecosystem model results. Also shown in Fig. 1 are the spatial distributions of 210 CO_2 and 73 $^{13}CO_2$ observation sites selected in this study from the NOAA GLOBALVIEW database. Most $^{13}CO_2$ sites except 11 are collocated with CO_2 sites.

2.1.2 Synthesis Bayesian inversion with CO_2 observations

To estimate the CO_2 flux ($\mathbf{f}$), we represent the relationship between CO_2 measurements and the flux from the surface by a linear model:

$$\mathbf{c} = \mathbf{G}\mathbf{f} + \mathbf{A}c_0 + \varepsilon \quad (1)$$

ACPD
13, 26529–26578, 2013

where $\boldsymbol{c}_{m\times 1}$ is a given vector of m CO_2 concentration observations over space and time (m equals number of stations times number of months, and for CO_2 only inversion, it is 12600, i.e. 210 stations ×60 months); $\boldsymbol{\varepsilon}_{m\times 1}$ is a random error vector with a zero mean and a covariance matrix $\mathrm{cov}(\boldsymbol{\varepsilon}) = \mathbf{R}_{m\times m}$; $\mathbf{G}_{m\times(n-1)}$ is a matrix representing a transport (observation) operator, where $n-1$ is the number of fluxes to be determined (equals 3000, i.e. 50 regions × 60 months); $\boldsymbol{A}_{m\times 1}$ is a unity vector (filled with 1) related to the assumed initial well-mixed atmospheric CO_2 concentrations (c_0) before the first month; and $\boldsymbol{f}_{(n-1)\times 1}$ is an unknown vector of monthly carbon fluxes of all studied regions.

Combining matrixes $\mathbf{G}$ and $\mathbf{A}$ as $\mathbf{M}_{m\times n} = (\mathbf{G}, \mathbf{A})$ and vectors $\mathbf{f}$ and c_0 as $\boldsymbol{s}_{n\times 1} = (\mathbf{f}^{\mathrm{T}} c_0)^{\mathrm{T}}$, Eq. (1) can be expressed as

$$\mathbf{c} = \mathbf{M}\mathbf{s} + \boldsymbol{\varepsilon} \tag{2}$$

The inverse problem of estimating $\mathbf{s}$ from $\mathbf{c}$ is often poorly constrained and a Bayesian approach is used to circumvent this problem. Pre-existing knowledge and models incorporating additional sources of information can be used to provide an initial estimate of $\mathbf{s}$, known as the a priori, to constrain the inverse problem. This a priori is then updated when it is combined with information from $\mathbf{c}$ measurement to form posterior estimate of $\mathbf{s}$, known as the a posteriori. In Bayesian synthesis inversion (Tarantola, 1987), the following objective function is employed in the place of the traditional least square objective function:

$$\mathbf{J} = \frac{1}{2}(\mathbf{M}\mathbf{s} - \mathbf{c})^{\mathrm{T}}\mathbf{R}^{-1}(\mathbf{M}\mathbf{s} - \mathbf{c}) + \frac{1}{2}(\mathbf{s} - \mathbf{s}_{\mathrm{p}})^{\mathrm{T}}\mathbf{Q}^{-1}(\mathbf{s} - \mathbf{s}_{\mathrm{p}}) \tag{3}$$

where $\boldsymbol{s}_{\mathrm{p},n\times 1}$ is the a priori estimate of $\mathbf{s}$; the covariance matrix $\mathbf{Q}_{n\times n}$ represents the uncertainty in the a priori estimate; and $\mathbf{R}_{m\times m}$ is the transport model-data mismatch error covariance. By minimizing this objective function expressed in Eq. (3), we obtain the posterior best estimate of $\mathbf{s}$ as (Enting, 2002):

$$\hat{\mathbf{s}} = (\mathbf{M}^{\mathrm{T}}\mathbf{R}^{-1}\mathbf{M} + \mathbf{Q}^{-1})^{-1}(\mathbf{M}^{\mathrm{T}}\mathbf{R}^{-1}\mathbf{c} + \mathbf{Q}^{-1}\mathbf{s}_{\mathrm{p}}). \tag{4}$$

ACPD
13, 26529–26578, 2013

Meanwhile the posterior uncertainty matrix for the posterior flux can be deduced as follows:

$$\hat{\mathbf{Q}} = (\mathbf{Q}^{-1} + \mathbf{M}^{\mathrm{T}}\mathbf{R}^{-1}\mathbf{M})^{-1}. \tag{5}$$

We employ the sum of squares of normalized residuals of optimized CO_2 and $^{13}CO_2$ after the inversion relative to observations to perform a χ^2 test to the consistency of the fit to data and prior flux estimates simultaneously (Gurney et al., 2003).

2.1.3 Synthesis Bayesian inversion with both CO_2 and $^{13}CO_2$ observations

We attempt to use $^{13}CO_2$ observations to provide an additional constraint to the otherwise CO_2-only inversion presented above. This additional constraint is possible on the grounds that air $^{13}CO_2$ concentration is affected differently by carbon fluxes through the ocean and land surfaces. Since the $^{13}CO_2$ gas is transported passively in the same way as CO_2, the same transport matrix **M** applies to $^{13}CO_2$ data to associate $^{13}CO_2$ observations with the surface $^{13}CO_2$ flux. In order to conduct an inversion using both CO_2 and $^{13}CO_2$ observations, we simply append $^{13}CO_2$-related data to the **c**, **R** and **M** matrixes in Eq. (4), while the **s** matrix remains unchanged as the purpose of this joint inversion is only to improve the CO_2 flux. For **c** and **R**, $^{13}CO_2$ observations and their variances are appended directly to the original matrixes for the CO_2 only case, as shown in Eq. (6). Similarly, the **M** matrix is also extended to consider $^{13}CO_2$ transport, and the relevant elements for the $^{13}CO_2$ observation stations are from the original **M** matrix. However these elements are multiplied by a ratio of the CO_2 to the $^{13}CO_2$ flux for each station and each month in order to convert the $^{13}CO_2$ flux into the CO_2 flux. The underlying assumption of this mathematical treatment is that the ratio of these two prior fluxes is not affected by the inversion process, i.e., the posterior ratio is the same as the prior ratio. The extended **M** is a combination of the corrected **M** matrix appended to the **M** matrix for CO_2 (see

ACPD
13, 26529–26578, 2013

$$\begin{bmatrix} M_{1,1} & M_{1,2} & \cdots & M_{1,n} \\ M_{2,1} & M_{2,2} & \cdots & M_{2,n} \\ \cdots & \cdots & & \\ M_{m,1} & M_{m,2} & \cdots & M_{m,n} \\ W_{m+1,1} & W_{m+1,2} & \cdots & W_{m+1,n} \\ W_{m+k,1} & W_{m+k,2} & \cdots & W_{m+k,n} \end{bmatrix} \begin{bmatrix} s_1 \\ s_2 \\ \\ \\ \\ s_n \end{bmatrix} = \begin{bmatrix} c_1 \\ c_2 \\ \\ c_m \\ c_{m+1} \\ c_{m+k} \end{bmatrix}$$

All available CO_2 data

73 stations' ^{13}C data

below) where c_i is the CO_2 concentration (i = 1 to m) and $^{13}CO_2$ concentration ($i = m+1$ to $m+k$) from the starting month (i = 0); M_{ij} is the transport operator between region j and station i; and $W_{ij} = R_j M_{ij}$, in which R_j is the ratio of the $^{13}CO_2$ to the CO_2 flux for region j.

For ocean regions, R_j is calculated with following formula (Ciais et al., 1995b):

$$R_j = R_{fo,j} = S_{o,j}(^{13}C)/S_{o,j}(CO_2) = \alpha_{ao,j}R_a + \alpha_{ao,j}F_{oa,j}(R_{oe,j} - R_a)/S_{o,j}(CO_2) \quad (6)$$

where $S_{o,j}(^{13}C)$ is the ocean net $^{13}CO_2$ net flux in region j, $S_{o,j}$ (CO_2) is the ocean net CO_2 flux, $\alpha_{ao,j}$ is the atmosphere-to-ocean fractionation, R_a is the $^{13}C/^{12}C$ ratio in the atmosphere (‰), $F_{oa,j}$ is the one way ocean-to-atmosphere CO_2 flux, and $R_{oe,j} = (\alpha_{oaj}/\alpha_{ao,j})R_o$, where R_o is the $^{13}C/^{12}C$ ratio in the ocean (‰) and $\alpha_{oa,j}$ is the ocean-to-atmosphere fractionation calculated with sea surface temperature (Ciais et al., 1995b; Enting et al., 1993). Actually, $(R_{oe,j} - R_a)$ is the disequilibrium between the atmosphere and the ocean. In order to avoid excessively large values for the second term in Eq. (7) when $S_{o,j}$ (CO_2) is close to zero, we limit the second term to within the range of ±2 ‰ R_a, resulting in $R_{fo,j}$ in the range from 0.0111473 to 0.0111024.

ACPD
13, 26529–26578, 2013

For land regions, R_j is calculated with a similar formula (Ciais et al., 1995b):

$$R_j = R_{\mathrm{fb},j} = S_{\mathrm{b},j}(^{13}\mathrm{C})/S_{\mathrm{b},j}(\mathrm{CO_2}) = -\alpha_{\mathrm{ph},j}R_{\mathrm{a}} + \alpha_{\mathrm{ph},j}S_{\mathrm{resp},j}(R_{\mathrm{be},j} - R_{\mathrm{a}})/S_{\mathrm{b},j}(\mathrm{CO_2}) \quad (7)$$

where $S_{\mathrm{b},j}(^{13}\mathrm{C})$ is the biosphere net $^{13}\mathrm{CO_2}$ flux in region j; $S_{\mathrm{b},j}(\mathrm{CO_2})$ is the biosphere net $\mathrm{CO_2}$ flux, and $\alpha_{\mathrm{ph},j}$ is the photosynthesis fractionation, defined as $\alpha_{\mathrm{ph},j} = 1 - (\delta_a - \Delta_j)$, where δ_{a} is the isotopic composition of current atmosphere $\mathrm{CO_2}$ (8 ‰) and Δ_j is the photosynthesis discrimination; R_a is the $^{13}\mathrm{C}/^{12}\mathrm{C}$ ratio in the atmosphere (‰); and $(R_{\mathrm{be},j} - R_{\mathrm{a}})$ is the disequilibrium between the atmosphere and the biosphere. Δ_j, $S_{\mathrm{resp},j}$ and $(R_{\mathrm{be},j} - R_a)$ are simulated with the BEPS model to be described below. In the implementation of Eq. (8), we limit the second term within the range of ±2 ‰ R_{a} to avoid its extreme values when $S_{\mathrm{b},j}(\mathrm{CO_2})$ is close to zero.

In order to investigate the influences of the isotopic discrimination and disequilibrium over land and ocean on the inversion results, we conduct six sets of inversions for the following six cases: Case I: variable ratios are used for 11 ocean and 39 land regions as calculated with Eqs. (7) and (8) that consider the spatial variations of $\mathrm{CO_2}$ and $^{13}\mathrm{CO_2}$ fluxes and the isotopic disequilibrium. This is the ideal case as a basis to investigate other cases; Case II: the ratio for ocean regions is variable (same as Case I), but the ratio over land is taken as a constant of 0.010934 (−27 ‰), which is taken as the sum of average $\delta^{13}\mathrm{C_a}$ (−8 ‰) and average photosynthesis discrimination Δ_j (−19 ‰). This is a case to ignore regional differences in isotopic discrimination and disequilibrium over land; Case III: the ratio for land regions is taken as a constant (same as Case II) and the ratio for ocean regions is also taken as a constant, being 0.011125 (−10 ‰) taken as the sum of $\delta^{13}\mathrm{C_a}$ (−8 ‰) and average ocean discrimination (−2 ‰). This is a case to ignore the regional differences in isotopic discrimination and disequilibrium over both land and ocean. Case IV: the ratios for ocean regions remain the same as Case I, but the ratios for land regions are determined by photosynthetic discrimination only, i.e. the first term in Eq. (8). This is a case to ignore the isotopic disequilibrium between photosynthesis and respiration over land; Case V: the ratios for land regions remain the same as Case I, but the ratios for ocean regions are determined by the first

ACPD
13, 26529–26578, 2013

term in Eq. (7). This case ignores ocean disequilibrium; and Case VI: both land and ocean disequilibrium are ignored, but all others are same as Case I.

The $^{13}CO_2$ concentration time series ($c_{m+1}, \ldots c_{m+k}$) in Eq. (6) is determined as follows:

$$c_i = {}^{13}C_{\mathrm{obs},i} - \sum_{k=1}^{4} {}^{13}C_{k,i} - {}^{13}C_{\mathrm{var},i} \tag{8}$$

where ${}^{13}C_{\mathrm{obs},i}$ is the concentration of $^{13}CO_2$ at observation station i, calculated with the following equation:

$${}^{13}C_{\mathrm{obs},i} = ({}^{13}\delta_{\mathrm{obs},i} \cdot 0.001 + 1) \cdot R_{\mathrm{PDB}} \cdot C_{\mathrm{obs},i} \tag{9}$$

where ${}^{13}\delta_{\mathrm{obs},i}$ is the observed $^{13}CO_2/CO_2$ ratio in per mil (‰), R_{PDB} is the standard $^{13}CO_2/CO_2$, and $C_{\mathrm{obs},i}$ is observed CO_2 concentrations. The second term in the right side of Eq. (9), $\Sigma^{13}C_{k,i}$, is the sum of $^{13}CO_2$ concentration increments due to emissions from fossil fuel, ocean, biosphere and fire. The details for these data are given in the following sections (2.2, 2.3 and 2.4). The third term in the right side of Eq. (9), ${}^{13}C_{\mathrm{var},i}$, accounts for the small variation in the observed $^{13}CO_2$ due to the temporal variation in CO_2 concentration. Its value at t time step is calculated from:

$${}^{13}C_{\mathrm{var},i}(t) = [C_{\mathrm{a}}(t) - C_{\mathrm{a}}(t-1)] \cdot R_{\mathrm{a}} \tag{10}$$

where $C_{\mathrm{a}}(t-1)$ and $C_{\mathrm{a}}(t)$ are the CO_2 concentrations at $t-1$ and t, respectively, and R_a is the average $^{13}CO_2/CO_2$ ratio of the atmosphere between $t-1$ and t.

2.1.4 Covariance matrixes for the CO_2 flux and CO_2 and $^{13}CO_2$ concentration measurements

In the joint inversion using both CO_2 and $^{13}CO_2$ measurements, the covariance matrix (**Q**) for the CO_2 flux remains the same as that in the CO_2 only inversion (Eq. 3) but

ACPD
13, 26529–26578, 2013

the error matrix (**R**) for concentration measurements is expanded to the dimension of 16980 × 16980 to include 60 months of $^{13}CO_2$ observations at 73 stations. Following Deng and Chen (2011), we use an uncertainty of 2.0 Pg C yr^{-1} for the total global land surface CO_2 flux, and this total uncertainty is spatially distributed to the 39 regions according to the annual total NPP of these regions simulated by BEPS. For each region, the annual total uncertainty is further distributed to each month according to the simulated seasonal variation in NPP. The uncertainty for the total ocean flux is prescribed as 0.67 Pg C yr^{-1} (Deng and Chen, 2011). In this way, all the diagonal elements (Q_{ii}) in the uncertainty matrix **Q** are determined, while off-diagonal values are assigned to zero, i.e. no flux covariances between regions and months are assumed. The uncertainty of CO_2 measurements in the **R** matrix is the same as that described in Deng and Chen (2011), following the approach of Peters et al. (2005) and Bakers et al. (2006). In this approach, the uncertainty of a monthly CO_2 measurement at a site is estimated as $R_{ii} = \sigma^2_{\text{const}} + \text{GVsd}^2$, where constant portion σ_{const} in ppm is assigned according to site location: Antarctic (0.15), oceanic (0.30), land and tower (1.25), mountain (0.90), and aircraft (0.75), while the site-specific variable portion GVsd is obtained from the GLOBALVIEW-CO2 2008 database. The $^{13}CO_2$ measurement uncertainty in the unit of ppm is calculated in a similar way: the constant portion is taken as $R_a\sigma_{\text{const}}$, where R_a is the ratio of $^{13}CO_2$ to CO_2 in the air (~ 0.0112372), while the variable portion is obtained from the GLOBALVIEW-13CO2 2008 database after converting the unit from permil (‰) to ppm.

2.2 Prior CO_2 and $^{13}CO_2$ flux estimation

2.2.1 CO_2 flux

Terrestrial biosphere fluxes

A process-based terrestrial ecosystem model called the Boreal Ecosystem Productivity Simulator (BEPS) (Chen et al., 1999; Liu et al., 1997) is used in this study to estimate

ACPD
13, 26529–26578, 2013

the net terrestrial CO_2 flux and its components including the gross primary productivity (GPP), net primary productivity (NPP), heterotrophic respiration (S_{resp}), and net ecosystem productivity (NEP). GPP is calculated using the Farquhar's leaf-level model (Farquhar et al, 1980) upscaled to the canopy level using a recently refined two-leaf approach (Chen et al., 2012). NPP is taken as 45 % of GPP (Ise et al., 2010) as global biomass data and its components (stem, foliage, root) are lacking for reliable computation of the autotrophic respiration. S_{resp} is calculated as the sum of the decompositional CO_2 release from 9 soil carbon pools, namely coarse and dead wood detritus pool, surface structural pool, surface metabolic pool, surface microbial pool, fine-root structural litter pool, fine-root metabolic pool, soil microbial pool, slow carbon pool, and passive carbon pool. The sizes of these pools for each cover type in each 1° grid are estimated using a model spin-up approach based on simulated NPP in 2000 to create a global land sink of 3.73 Pg C yr^{-1}. The total NPP for each 1° grid is taken as a weighted sum of NPP of 7 aggregated land cover types, and the weights are proportional to the areal fractions of the cover types determined using the GLC2000 land cover map at 1 km resolution (Chen et al., 2012). Remotely sensed LAI (Deng et al., 2006) at 1 km resolution and a clumping index map at 6 km resolution (Chen et al., 2005) and a soil textural map (Webb et al., 1991) are aggregated to 1° grids for each cover type based on GLC2000 land and used as input to BEPS driven by National Center of Environmental Prediction (NCEP) reanalyzed data (Kalnay et al., 1996; Kanamittsu et al., 2002) are main input to BEPS to simulated hourly carbon fluxes.

Ocean fluxes

The daily flux of CO_2 across the air–water interface used in this study is constructed based on the results of daily CO_2 fluxes simulated by the OPA-PISCES-T model (Buitenhuis et al., 2006). This model is a global ocean general circulation model (OPA) (Madec et al., 1998) coupled to an ocean biogeochemistry model (PISCES-T) (Aumont et al., 2003; Buitenhuis et al., 2006). PISCES-T represents the full cycles of C, O_2, P, Si, total alkalinity and a simplified Fe cycle. It also includes a representation of

ACPD
13, 26529–26578, 2013

two phytoplankton, two zooplankton and three types of dead organic particles of different sinking rates. OPA-PISCES-T is forced by daily wind stress and heat and water fluxes from the NCEP reanalyzed data (Kalnay et al., 1996; Kanamittsu et al., 2002). Hourly $S_o(^{13}C)$ is calculated with gridded optimum interpolation sea surface temperature of NOAA National Climate Data Center (Reynolds and Smith, 1994; Reynolds et al., 2002).

Fossil-fuel emissions

The fossil fuel emission field (2000–2004) used in this study (http://carbontracker.noaa.gov) is constructed based on (1) the global, regional and national fossil-fuel CO_2 emission inventory from 1871 to 2006 (CDIAC) (Marland et al., 2009) and (2) the EDGAR 4 database for the global annual CO_2 emission on a 1° grid (Olivier et al., 2005). The $^{13}CO_2$ flux from fossil-fuel consumption is calculated from CO_2 emissions of different fuel types multiplied by their respective $^{13}C/^{12}C$ ratios with consideration of their latitudinal distributions based on Andres et al. (2000).

Fire emissions

CO_2 emissions due to vegetation fires are an important part of the carbon cycle (van der Werf et al., 2006). Each year, vegetation fires emitted around or more than 2 Pg C of CO_2 into the atmosphere, mostly in the tropics. The fire emission field used in this study is based on the Global Emissions Fire Database version 2 (GFEDv2) (Randerson et al., 2007; van der Werf et al., 2006)

2.2.2 $^{13}CO_2$ flux

Based on the initial work of Chen et al. (2006), BEPS is further developed to include a capacity to compute the global distribution of the terrestrial $^{13}CO_2$ flux. Following the principle of multi-stage ^{13}C fractionation in the pathway through leaf boundary layer,

ACPD
13, 26529–26578, 2013

stomates, messophyll and chloroplast initially proposed by Farquhar et al. (1984, 1989) and implemented globally by Suits et al. (2005), we developed a module in BEPS for computing the total photosynthetic fractionation and the resultant $^{13}CO_2$ flux. Specifically, the photosynthetic discrimination for C3 plants (Δ_{PC3}) is calculated from

$$\Delta_{PC3} = \frac{pA}{C_a}\left[\frac{\Delta_b}{g_b} + \frac{\Delta_s}{g_s} + \frac{\Delta_{diss} + \Delta_{aq}}{g_m}\right] + \frac{C_c}{C_a}\Delta_f \tag{11}$$

where Δ_b, Δ_s, Δ_{diss}, Δ_{aq}, and Δ_f are the rates of discrimination against $^{13}CO_2$ through leaf boundary layer, stomates, dissolution in mesophyll water, transport in aqueous phase, and fixation in chloroplast, respectively, and are assigned values of 2.9 ‰, 4.4 ‰, 1.1 ‰, 0.7 ‰ and 28.2 ‰, respectively (Suits et al., 2005). A is the photosynthetic rate in mol m^{-2} s^{-1} and p equals to $0.022624T_a/(273.16P)$ with the dimension of m^3 mol^{-1}, where T_a is air temperature in K and P is the standard air pressure at 1.013 bar. C_a and C_c are the CO_2 concentrations in mol mol^{-1} in the free air and leaf chloroplast, respectively. For C4 plants, the photosynthetic discrimination (Δ_{PC4}) is taken as a constant of 4.4 ‰ (Suits et al., 2005).

The leaf boundary-layer (g_b) is calculated with the following equation

$$g_b = \frac{\alpha N}{0.5l} \tag{12}$$

where α is the diffusivity of CO_2 in dry air in m^2 s^{-1} calculated as $10^{-6}(0.129+0.007T_a)$ and T_a is the air temperature in °C; l is the leaf characteristic dimension in m, taken as a constant of 0.1 m; and N is the Nusselt number equal to $(u_d l/\upsilon)^{0.5}$, where u_d is the wind speed in m s^{-1} at the vegetation displacement height (80 % of the average vegetation height) and υ is the kinematic viscosity of dry air in m^2 s^{-1} calculated as $10^{-6}(0.133+0.007T_a)$. u_d is derived from the wind speed above the canopy based on LAI and vegetation height assigned according to plant functional type (Table 1).

ACPD
13, 26529–26578, 2013

As part of the GPP calculation, the stomatal conductance (g_s) computed separately for sunlit and shaded leaves using the Ball–Berry equation (Ball, 1988),

$$g_s = f_w \left(m \frac{A h_s}{C_s} p + b \right) \tag{13}$$

where f_w is a scaling factor depending on soil moisture and texture (Chen et al., 2012); h_s is the air humidity at the leaf surface; C_s is the CO_2 concentration at the leaf surface; p is the same as in Eq. (12); and m and b are the slope and intercept in this linear relationship, and they are assigned values according to plant function type (Table 1) (Chen et al., 2012).

The mesophyll conductance g_m is calculated based on the method of Harley (1992):

$$g_m = \frac{A}{C_i - \frac{\Gamma \cdot [J + 8 \cdot (A + R_d)]}{J - 4 \cdot (A + R_d)}} \tag{14}$$

where A is the photosynthetic CO_2 assimilation rate; C_i is partial pressure of CO_2 in the air spaces inside leaves; R_d is the respiration rate occurring during the day not related to photorespiration; A is the CO_2 compensation point in the absence of R_d; and J is the rate of photosynthetic electron transport. These parameters are the same as those used in computing the CO_2 flux.

Our methods of computing stomatal and mesophyll conductances differ from previous studies (Suits et al., 2005; Scholz et al., 2008; Rayner et al., 2008) in the following ways: (1) these conductances are calculated separately for sunlit and shaded leaves because BEPS is a two-leaf model, in which the total GPP of a canopy is taken as the sum of sunlit and shaded leaf GPP; and (2) the mesophyll conductance mechanistically depends on a set of parameters rather than being treated as a constant or a value proportional to the stomatal conductance. Since it has been demonstrated that sunlit and shaded leaf separation is essential for accurate modeling of canopy-level photosynthesis (Chen et al., 1999; Sprintsin et al., 2011), it is expected that this separation

ACPD
13, 26529–26578, 2013

is also essential for $^{13}CO_2$ flux estimation. We found that the use of Harley's method for computing the mesophyll conductance makes the calculation of the ^{13}C photosynthetic fractionation stable for its global application, while the simpler method of treating the mesophyll conductance in proportion with the stomatal conductance often incurs abnormally large or small values of ^{13}C photosynthetic fractionation.

The photosynthetic $^{13}CO_2$ flux is in disequilibrium with the respiratory $^{13}CO_2$ flux because of the change in atmospheric $^{13}CO_2$ concentration since the preindustrial time (Ciais et al., 1995b; Fung et al., 1997). The heterotrophic respiratory flux from the decomposition of organic matter of different ages carries the memory of the past atmospheric $^{13}CO_2$ concentration, while the photosynthetic $^{13}CO_2$ flux is affected by the current atmospheric $^{13}CO_2$ concentration. Since one objective of our study is to utilize $^{13}CO_2$ data for differentiating terrestrial photosynthetic and respiration, much attention is given to this disequilibrium in this study. The isotopic composition of each of the 9 soil carbon pools ($\delta^{13}C_{\mathrm{soil},i}$) is estimated with following formula:

$$\delta^{13}\mathrm{C}_{\mathrm{soil},i} = \delta^{13}\mathrm{C}_{\mathrm{a}}(2003 - \tau_i) - \Delta \tag{15}$$

where $\delta^{13}\mathrm{C}_{\mathrm{a}}$ is the isotopic composition of carbon in atmosphere CO_2 in the past as determined by the ice-cord record (Francey et al., 1999); Δ is the annual mean of photosynthetic discrimination in 2003; τ_i is the age of carbon pool i (Table 2) (Ju et al., 2005). The mean $\delta^{13}\mathrm{C}_{\mathrm{soil}}$ is taken as the flux-weighted $\delta^{13}\mathrm{C}_{\mathrm{soil},i}$ for the 9 carbon pools. The results of $\delta^{13}\mathrm{C}_{\mathrm{soil}}$ for the globe are shown in Fig. 5.

2.3 Transport modeling

A transport-only version of the atmospheric chemistry and transport model TM5 (Krol et al., 2003, 2005) is used for CO_2 and $^{13}CO_2$ transport modeling to produce a fully linear operator on these fluxes. Tracer transport (advection, vertical diffusion, cloud convection) in TM5 is driven by offline meteorological fields taken from the European Centre

ACPD
13, 26529–26578, 2013

for Medium Range Weather Forecast (ECMWF) model. All physical parameterizations in TM5 are kept the same as the ECMWF formulation to achieve compatibility between them. The four background fluxes from terrestrial ecosystems, oceans, fossil-fuel burning, and biomass burning are individually inputted to TM5 to calculate the contributions of these fluxes to the atmospheric CO_2 and $^{13}CO_2$ concentrations.

2.4 CO_2 and $^{13}CO_2$ datasets

Monthly CO_2 and $^{13}CO_2$ concentration data from 2000 to 2004 are compiled from the GLOBALVIEW CO_2 and $^{13}CO_2$ database. Though the GLOBALVIEW database consists of both extrapolated and interpolated data that were created based on the technique devised by Masarie and Tans [1995], we selected the synchronized and smoothed values of actual observations to compile our concentrations datasets. To minimize the nonlinear aggregation effects of the large regions (Pickett-Heaps, 2007), the contributions of the four background fluxes are subtracted from the above monthly concentrations. So the matrix **c** in Eqs. (3) and (4) is expressed as

$$\mathbf{c} = \mathbf{c}_{obs} - \mathbf{c}_{ff} - \mathbf{c}_{bio} - \mathbf{c}_{ocn} - \mathbf{c}_{fire} \tag{16}$$

where $\mathbf{c}_{obs}$ is the monthly CO_2 and $^{13}CO_2$ concentrations obtained from GLOBALVIEW, and $\mathbf{c}_{ff}$, $\mathbf{c}_{bio}$, $\mathbf{c}_{ocn}$, and $\mathbf{c}_{fire}$ are simulated contributions of CO_2 and $^{13}CO_2$ concentrations from the terrestrial biosphere, ocean, fossil-fuel, and fire fluxes, respectively.

3 Results

3.1 Prior CO_2 and $^{13}CO_2$ fluxes

Terrestrial ecosystem models integrate many sources of information, including vegetation structure, soil, and meteorology, to estimate carbon exchange of the land surface. Prior CO_2 and $^{13}CO_2$ fluxes produced by a model can therefore provide indispensible

ACPD
13, 26529–26578, 2013

constraints to the otherwise ill-posed inversion based CO_2 and $^{13}CO_2$ concentration observations alone. Depending on the assigned relative magnitudes of the error matrixes of these concentration observations and these prior fluxes (i.e., **R** and **Q** in Eq. 3), these prior fluxes can have equal or even dominant importance to these concentration observations in the inversion results. We have therefore paid a great attention in modeling these prior fluxes, in order to minimize the total inversion errors. Figure 2a shows an example of the global terrestrial GPP distribution in 2003 modeled by BEPS. The total GPP in this year is $132 \pm 22\,\mathrm{Pg\,C\,yr^{-1}}$ (Chen et al., 2012). This value is larger than some of the recent estimates, such as $123\,\mathrm{Pg\,C\,yr^{-1}}$ by Beer et al. (2010), mostly because the LAI values used as input to BEPS are generally larger than those of the MODIS product (Garrigues et al., 2008). Our LAI values are larger because we used a global clumping index map derived from a multi-angle satellite sensor POLDER (Chen et al., 2005). Clumping increases shaded leaves which contributed about 35 % to the total GPP globally. Without considering this clumping effect, the shaded leaf area is underestimated, resulting in an underestimation of the global GPP by 9 % (Chen et al., 2012). As the spatial distribution of clumping is not uniform (boreal and tropical forests are most clumped and crops and grasses are least clumped), this refinement in the GPP spatial distribution would have some effects on the inversion results between regions.

The net ecosystem productivity (NEP), the difference between GPP and ecosystem respiration, modeled by BEPS, is shown in Fig. 2b for 2003. Even though GPP has a large uncertainty (globally $22\,\mathrm{Pg\,C\,yr^{-1}}$ by BEPS), the uncertainty in NEP is much smaller (globally $2\,\mathrm{Pg\,C\,yr^{-1}}$ by BEPS) because a model spin-up approach is used to estimate the soil carbon pool sizes based on a dynamic equilibrium assumption. Under this assumption, the annual heterotrophic respiration (S_{resp}) equals annual NPP during the preindustrial period, and the soil carbon pool sizes are derived from S_{resp} by solving a set of differential equations describing the decomposition and interactions among the pools (Govind et al., 2011). In this way, S_{resp} is forced to depend on NPP and the systematic biases in GPP are not carried into NEP estimation. NEP is non-

ACPD
13, 26529–26578, 2013

zero after the preindustrial period because of the changes in climate and atmospheric composition (CO_2 and nitrogen) as well as disturbance. In our regional modeling, both disturbance and non-disturbance effects are considered for Canada (Chen et al., 2003) and USA (Zhang et al., 2012) forests. However, in our global model spin-up from 1901 (taken as the end of preindustrial period) to 2000, only the non-disturbance effects are considered because of lack of spatially explicit disturbance data outside of North America, while carbon emission due to fire disturbance in the study period from 2000 to 2004 is considered separately using the GFED dataset (Randerson et al., 2007; van der Werf et al., 2006). The prior net CO_2 fluxes for the 50 regions for the years 2002–2004 are given in Table 3 with inversion results with and without the ^{13}C constraint.

The global distribution of the total photosynthetic discrimination ($\delta^{13}C_{pt} = \delta^{13}C_a - \Delta$) modeled by BEPS is shown in Fig. 3. Forests, such as those in North America, Russia, Europe, Amazon, central Africa, central China and southeast Asia, generally have high photosynthetic discrimination rates (> 16 ‰), while grassland and cropland (in particular C4 grasses and crops) have low discrimination rates. Also shown in Fig. 3 is the ocean diffusive discrimination against $^{13}CO_2$. The discrimination over ocean is much smaller than that over land. This difference between land and ocean discrimination may be considered as the largest signal of $^{13}CO_2$ observations on the global carbon cycle (Tans et al., 1990; Rayner et al., 2008) and is considered in our inversion using different $^{13}CO_2/CO_2$ flux ratios for ocean and land regions (see Eq. 6).

To estimate the disequilibrium between photosynthetic and respiratory discrimination against $^{13}CO_2$, the global distribution of the mean soil carbon age is computed after weighting the ages of the 9 soil carbon pools against their fluxes due to decomposition (Fig. 4). Forests at high latitudes have the soil carbon age of about 40–60 yr, while the tropical forests have much lower values in the range from 10 to 30 yr. This latitudinal distribution pattern is mostly determined by soil temperature. In low latitudes, high temperature induces fast turnovers of detritus and fast soil carbon pools, while at high latitudes, low temperature maintains relatively large fractions of slow and passive soil carbon pools. Cropland and grassland also have larger fractions of fast and

ACPD
13, 26529–26578, 2013

detritus carbon pools than forest cover types and therefore have younger soil carbon on average. This spatial distribution of soil carbon age has a strong influence on the total respiratory discrimination against ^{13}C ($\delta^{13}C_r$) calculated by BEPS (Fig. 5). Respiration from older carbon at high latitudes carries the memory of the older atmosphere with less $^{13}CO_2$ concentration and hence has lower discrimination rates (larger $\delta^{13}C_r$). However, respiration would mostly depend on the photosynthetic discrimination rates. As a result, forested areas have higher respiratory discrimination rates (lower $\delta^{13}C_r$). Most of the high values of $\delta^{13}C_r$ (smaller absolute values) in Fig. 5 are associated with large fractions of C4 plants in the grid, such as the corn belt in the USA, cropland in northeast China, southern border of Sahara desert, southeast South America. The global distribution of the disequilibrium between photosynthetic and respiratory discrimination, taken as the difference between Fig. 3 and Fig. 5, is shown in Fig. 6. The disequilibrium is the largest at the high latitude boreal forests in North America and Eurasia because their soil carbon is the oldest, as shown in Fig. 4. The spatial distribution pattern of the disequilibrium is similar to those of Ciais et al. (1995b) and Fung et al. (1997) but the magnitude is larger because the date of our result in 2000 is more recent than these two previous studies. As the time lapses, the atmosphere is getting lighter in terms of the isotopic composition of CO_2 resulting from the increased air-borne CO_2 from fossil fuel consumption. Also shown in Fig. 6 is the disequilibrium over the ocean estimated using the method of Ciais et al. (1995b). This ocean disequilibrium has a large latitudinal gradient because of the gradients in sea surface temperature gradient and the fluxes of CO_2 and $^{13}CO_2$. The spatial distribution in the disequilibrium and the differences in disequilibrium between ocean and land may be considered to be the secondary signal of $^{13}CO_2$ observations on the global carbon cycle. The effects of these disequilibria on the carbon flux are considered in our inversion through the use of region-specific $^{13}CO_2/CO_2$ flux ratios in Eq. (6), and the magnitudes of these effects are investigated through different treatments (cases) of this ratio as shown in the following section.

ACPD
13, 26529–26578, 2013

3.2 Inverse modeling results

3.2.1 Results with and without $^{13}CO_2$ constraint

To investigate the usefulness of $^{13}CO_2$ observations in inverse modeling of the CO_2 flux, we conducted inversions with and without $^{13}CO_2$ constraint as expressed in Eq. (6), i.e. with and without the ^{13}C-related expansions of the matrixes. Figures 7 and 8 show the result of a CO_2-only inversion (i.e. without $^{13}CO_2$ constraint) and the result of $CO_2 + {}^{13}CO_2$ inversion (i.e. with $^{13}CO_2$ constraint), respectively, as the net carbon flux over land and ocean averaged for the period of 2002–2004. These results with $^{13}CO_2$ constraint are obtained as Case I where the ratios for CO_2 and $^{13}CO_2$ for land and ocean are variable among regions according to the land and ocean models. Although the inversions were made for the 2000–2004 period, the results of the first two years are not included in the analysis because they are affected by the assumption of uniform CO_2 and $^{13}CO_2$ global distributions at the start of our transport modeling using TM5. An 18–24 month period is usually considered to be necessary for the simulated distributions to reach realistic states with reasonably accurate prior surface fluxes from ocean and land and atmospheric transport simulations (Rödenbeck et al., 2003; Deng and Chen, 2011). The general patterns of the inverted carbon flux are similar between these two inversions because these inversions depend primarily on the CO_2 concentration, the prior flux and the error matrixes of the prior flux and concentration observation. However, there are several notable differences: (1) the carbon source from the Amazon region is greatly reduced, and this reduction is compensated by an increased carbon source in the ocean region immediately west to Amazon and a decreased sink in the southeast Asian land region. These large changes brought by the inclusion of $^{13}CO_2$ in the inversion are likely caused by the relatively large addition of information from $^{13}CO_2$ in these tropical regions where CO_2 observations are sparse. The contrast in $^{13}CO_2$ discrimination between land and ocean is particularly effective in redistributing carbon fluxes between land and ocean; and (2) the Alaska region becomes a larger

ACPD
13, 26529–26578, 2013

carbon source with $^{13}CO_2$ constraint, and this is also likely caused by the fact that this region is in the vicinity of ocean and therefore most affected by the difference in the discrimination rate between ocean and land. There are also small changes for other smaller regions in North America (Fig. 9). Under the $^{13}CO_2$ constraint, most regions in North America show a small increase in sink, and their overall sink increases from 0.67 to 0.71 $Pg\,C\,yr^{-1}$.

The inverted results for the 21 large land and ocean regions with and without the $^{13}CO_2$ constraint are shown in Fig. 10. Most regions show small but noticeable changes in the inverted carbon sinks or sources except aforementioned regions 31 (Amazon), 37 (Southeast Asia) and 41 (ocean region west of Amazon). These large and small changes modified significantly the inverted overall land and ocean sinks (Fig. 11). The land sink increases from 3.4 ± 0.84 to 3.70 ± 0.81 $Pg\,C\,yr^{-1}$, while the ocean sink decreases from 1.48 ± 0.40 to 1.12 ± 0.38 $Pg\,C\,yr^{-1}$. These land sink estimates do not include the emission due to fire. The mean fire emission is 2.25 $Pg\,C\,yr^{-1}$ over the 2002–2004 period, and the net land sink is the inverted land sink less this amount due to fire emission.

While the information content of $^{13}CO_2$ observations in terms of the difference in discrimination between land and ocean appears to have large impacts on the inversion results for several regions, the usefulness of these observations for refining the spatial distribution of the carbon flux over land is less certain.

3.2.2 Results with different treatments of the $^{13}CO_2/CO_2$ flux ratio

The inversion results with $^{13}CO_2$ constraint shown in Fig. 8 are from Case I with the best estimates of the $^{13}CO_2/CO_2$ flux ratio and therefore represent a baseline study to which other cases are compared for the purpose of investigating the importance of accurate consideration of the spatial distributions of isotopic discrimination and disequilibrium.

ACPD
13, 26529–26578, 2013

Case II is designed to investigate the importance of using an accurate spatial distribution of the photosynthetic isotopic discrimination for inverting the CO_2 flux by forcing the $^{13}CO_2/CO_2$ flux ratio to be constant over land, while the ocean discrimination remains spatially variable. Figure 12a shows the spatial distribution of the difference in this ratio among 39 land regions between Case I and Case II. Regions with negative differences in the flux ratio are shown with negative differences in the inverted CO_2 flux, meaning larger sinks, and vice versa. This is because a smaller $^{13}CO_2/CO_2$ flux ratio means a larger CO_2 flux from the atmosphere to the surface (larger negative value) for the same $^{13}CO_2$ flux under the condition that the prior flux is negative (sink). Under the same condition, a larger $^{13}CO_2/CO_2$ flux ratio induces a smaller sink (less negative). While regional differences between Case I and Case II can be quite large, e.g. up to $10\,g\,C\,m^{-2}\,yr^{-1}$ or 25 % of the sink in the Amazon area (Region 31), changes of the global sink values from Case I to Case II are small (Table 3): from 3.70 ± 0.81 to $3.66 \pm 0.81\,Pg\,C\,yr^{-1}$ for land and from 1.12 ± 0.38 to $1.17 \pm 0.39\,Pg\,C\,yr^{-1}$ for ocean.

Case III shows the consequence in flux inversion if the spatial distribution of the $^{13}CO_2/CO_2$ flux ratio is ignored over both ocean and land regions, similar to the case of double deconvolution at the global scale using the global mean values of discrimination for land and ocean separately. In this case, the ratio over land is the same as that in Case II, but the ratio over ocean differs significantly from that in Case I (Fig. 12c) because of the large variations of this ratio among ocean regions. The difference in the inverted CO_2 flux between Case I and Case III (Fig. 12d) is similar that that between Case I and Case II (Fig. 12b). Noticeable differences between these two difference maps are: Fig. 12d shows a larger sink in Amazon, smaller sinks in Europe and Russia, and a smaller source in North Africa, indicating that ignoring the small spatial variation of the $^{13}CO_2$ discrimination rate over ocean can have noticeable influence on the inverted sink over land. The total land sink decreases only slightly from $3.70 \pm 0.81\,Pg\,C\,yr^{-1}$ for Case I to $3.66 \pm 0.81\,Pg\,C\,yr^{-1}$ for Case III, and correspondingly the ocean sink increases also slight from $1.12 \pm 0.38\,Pg\,C\,yr^{-1}$ to $1.16 \pm 0.39\,Pg\,C\,yr^{-1}$ (Table 3). These results indicate that the double deconvolution method using constant

ACPD
13, 26529–26578, 2013

discrimination rates (or $^{13}CO_2/CO_2$ flux ratios) is reliable is in partitioning sinks between land and ocean, but the distribution of the sink over land can be significantly distorted (up to 25 % for some regions).

Case IV, Case V and Case VI are conducted to investigate the importance in considering the disequilibrium in the $^{13}CO_2$ flux over land and ocean for the CO_2 flux inversion. In Case IV, where the disequilibrium over land is ignored while other settings remain the same as Case I, the land sink increases by 0.010 Pg C yr^{-1}, while the ocean sink decreases by 0.010 Pg C yr^{-1} in comparison with Case I. When the disequilibrium over ocean is ignored (Case V), the land sink increases by 0.008 Pg C yr^{-1}, while the ocean sink decreases by 0.008 Pg C yr^{-1}, in comparison with Case I. When the disequilibria over both land and ocean are ignored, the land sink increases by 0.018 Pg C yr^{-1}, while the ocean sink decreases by 0.018 Pg C yr^{-1}, in comparison with Case I. Results from these case studies suggest that in the joint inversion using both CO_2 and $^{13}CO_2$ measurements, the inverted CO_2 flux is not sensitive to the existence of $^{13}CO_2$ disequilibra over land and ocean. This is because these disequilibria only modify slightly the $^{13}CO_2/CO_2$ flux ratio (R_j), i.e., in the formulation of Eq. (6) with $W_{ij} = R_j M_{ij}$, the disequilibria only influence slightly the magnitude of R_j and consequently the $^{13}CO_2$ concentration. This insensitivity of the inversion results to disequilibria suggest that our joint inversion methodology is not prone to the errors in the estimation of the disequilibria over land and ocean, and therefore the main utility of $^{13}CO_2$ measurement in the inversion is to provide a constraint on the partition between ocean and land sinks. This insensitivity also indicates that our inversion methodology has not fully utilized $^{13}CO_2$ measurement for differentiation between photosynthetic and respiratory fluxes over land, and this differentiation remains a challenge yet to be overcome. A different joint inversion strategy may be needed for this purpose.

ACPD
13, 26529–26578, 2013

4 Discussion

The overall effects of including $^{13}CO_2$ data in the inversion are small to moderate in terms of the total sinks to land and ocean, the partition between them, and their uncertainty reduction. This is may be because the number of $^{13}CO_2$ observation sites (73) is much smaller than that of CO_2 observation sites (210) and only 11 $^{13}CO_2$ observation sites are not collocated with CO_2 observations sites. The temporal and spatial samplings of $^{13}CO_2$ are therefore mostly correlated with those of CO_2, and as a result, the joint inversion is dominated by CO_2 measurements. However, because of the additional information of $^{13}CO_2$ for partitioning between ocean and land carbon fluxes, the inclusion of $^{13}CO_2$ data in the inversion is shown to induce some large and meaningful changes in the spatial distribution of the inverted carbon flux, as demonstrated in Case II and Case III relative to Case I.

The reduction of the uncertainty in the inverted CO_2 flux when $^{13}CO_2$ data are used is small ($\sim 3\,\%$) (Table 3). Since the relative error in $^{13}CO_2$ measurement is similar to that in CO_2 measurement, this small reduction in uncertainty may be indicative of the small additional information content of $^{13}CO_2$ measurements for CO_2 flux inversion. In the joint inversion, the uncertainty in the prior $^{13}CO_2$ flux estimation is not required, and therefore the posterior uncertainty in inverted CO_2 flux does not directly take into account of the error in the prior $^{13}CO_2$ flux estimation, although through the $^{13}CO_2/CO_2$ flux ratio used in the transport matrix (**M**) (Eq. 6), the prior $^{13}CO_2$ flux estimation has influence on the inversion results. Errors in modeling the spatial and temporal variations of the $^{13}CO_2$ flux stem from many sources including errors in modeling the discrimination, which is affected by the fractionation of the $^{13}CO_2$ flow through leaf boundary layer, stomata, mesophyll, etc., and the disequilibrium, which depends on the sizes of 9 soil carbon pools and their ages. Although the ocean $^{13}CO_2$ discrimination is small, but its disequilibrium has a strong latitudinal gradient, which is approximately calculated using the mean monthly temperature. The error in the calculated disequilibrium is

ACPD
13, 26529–26578, 2013

estimated to be ±0.6 ‰ for the monthly values at a given location and ±0.2 ‰ for the global annual total. Because of these errors, we estimate that the relative uncertainty in the prior $^{13}CO_2$ flux is similar to that of the prior CO_2 flux over both land and ocean.

For the 3 yr (2002–2004) included in this study, existing estimates (Le Quéré et al., 2009) for both oceanic and land carbon sinks are about 2 Pg C yr^{-1}. This land sink estimate also excludes fire emission. Although the prior estimates of these sinks in our inversions are similar to these values, our CO_2 only inversion considerably increases the land sink and decreases the ocean sink. The addition of $^{13}CO_2$ measurements in the inversion further increases the land sink and decreases the ocean sink, i.e. further away from the existing estimates. Although our inversion results may subject to considerable errors in atmospheric transport modeling and prior flux modeling, there seems to be a strong pull by the atmospheric signal towards a larger land sink and a smaller ocean sink than the existing estimates. This "unusual" behavior of atmospheric inversion may deserve further attention.

5 Conclusions

The usefulness of atmospheric $^{13}CO_2$ measurements at 73 stations for global carbon cycle estimation is explored through their use as an additional constraint on an atmospheric inversion of the surface carbon flux using CO_2 observations. The following conclusions are drawn from this study:

1. This ^{13}C constraint made significant changes to the inversion results of the CO_2 flux. These changes are the largest at tropical land and ocean areas where CO_2 observations are sparse, and therefore the additional signal from $^{13}CO_2$ data becomes most important. For the inversion period of 2002–2004, this $^{13}CO_2$ constraint increased the land sink from 3.397 ± 0.836 to 3.704 ± 0.809 Pg C yr^{-1} and decreases the total oceanic carbon sink from 1.482 ± 0.396 to 1.049 ± 0.385 Pg C yr^{-1} (Table 3).

ACPD
13, 26529–26578, 2013

2. The impact of $^{13}CO_2$ data on the CO_2 inversion is mostly caused by the large difference in isotopic discrimination between ocean and land. The spatial distributions of the $^{13}CO_2$ discrimination rate over both land and ocean have noticeable impacts on the spatial distribution of the CO_2 sink over land (up to 25 % in some regions), suggesting reliable models for simulating the spatial distributions of the ^{13}C discrimination rate over both land and ocean are needed for effective use of $^{13}CO_2$ data for global carbon cycle inversion.

3. The joint inversion methodology using both CO_2 and $^{13}CO_2$ measurements can effectively consider the difference in $^{13}CO_2$ discrimination between land and ocean for partitioning the carbon sink but is not sensitive to the disequilibrium in the $^{13}CO_2$ over both land and ocean. A different methodology is yet needed to make full use of the information content of isotopic disequilibrium for discriminating between photosynthetic and respiratory fluxes.

Acknowledgements. We greatly appreciate the GlobalView dataset that is available from the NOAA Climate Monitoring and Diagnostics Laboratory. NCEP/DOE 2 Reanalysis data are provided by the NOAA/OAR/ESRL PSD, Boulder, Colorado, USA, from their Web site at http://www.esrl.noaa.gov/psd/. This research was support by a grant (2010CB0704) from the Global Change Key Program of the Chinese Ministry of Science and Technology and a grant (GR-646) from the former Canadian Foundation for Climate and Atmospheric Sciences. Misa Ishizawa, Douglas Chan and Kaz Higuchi of Environment Canada provided useful suggestions and technical assistance at the beginning of the project, and Jonathan Fung assisted in the CO_2-only inversion during his M.Sc. studies.

References

Andres, R. J., Marland, G., Boden, T. T., and Bischof, S.: Carbon dioxide emissions from fossil fuel consumption and cement manufacture, 1751–1991, and an estimate of their isotopic composition and latitudinal distribution, in: The Carbon Cycle, edited by Wigley, T. M. L. and Schimel, D. S., Cambridge University Press, Cambridge, 53–62, 2000.

ACPD
13, 26529–26578, 2013

Aumont, O., Maier-Reimer, E., Blain, S., and Monfray, P.: An ecosystem model of the global ocean including Fe, Si, P colimitations, Global Biogeochem. Cy., 17, 1060, doi:10.1029/2001GB001745, 2003.

Baker, D. F., Law, R. M., Gurney, K. R., Rayner, P., Peylin, P., Denning, A. D., Bousquet, P., Bruhwiler, L., Chen, Y. H., Ciais, P., Fung, I. Y., Heimann, M., John, J., Maki, T., Maksyutov, S., Masarie, K., Prather, M., Pak, B., Taguchi, S., and Zhu, Z.: TransCom 3 inversion intercomparison: Impact of transport model errors on the interannual variability of regional CO_2 fluxes, 1988–2003, Global Biogeochem. Cy., 20, GB1002, doi:10.1029/2004GB002439, 2006.

Ball, J. T.: An Analysis of Stomatal Conductance, Ph. D. thesis, 89 pp., Stanford Univ., Stanford, Calif., 1988.

Beer, C., Reichstein, M., Tomelleri, E., Ciais, P., Jung, M., Carvalhais, N., Rodenbeck, C., Arain, M. A., Baldocchi, D., Bonan, G. B., Bondeau, A., Cescatti, A., Lasslop, G., Lindroth, A., Lomas, M., Luyssaert, S., Margolis, H., Oleson, K. W., Roupsard, O., Veenendaal, E., Viovy, N., Williams, C., Woodward, F. I., and Papale, D.: Terrestrial gross carbon dioxide uptake: global distribution and covariation with climate, Science, 329, 834–838, 2010.

Buitenhuis, E., Le Quéré, C., Aumont, O., Beaugrand, G., Bunker, A., Hirst, A., Ikeda, T., O'Brien, T., Piontkovski, S., and Straile, D.: Biogeochemical fluxes through mesozooplankton, Global Biogeochem. Cy., 20, GB2003, doi:10.1029/2005GB002511, 2006.

Canadell, J. G., Le Quéré, C., Raupach, M. R., Field, C. B., Buitenhuis, E. T., Ciais, P., Conway, T. J., Gillett, N. P., Houghton, R. A., and Marland, G.: Contributions to accelerating atmospheric CO_2 growth from economic activity, carbon intensity, and efficiency of natural sinks, P. Natl. Acad. Sci. USA, 104, 18866–18870, 2007.

Chen, B., Chen, J. M., Huang, L., and Tans, P.: Simulating dynamics of $^{13}CO_2$ in the planetary boundary layer over a boreal forest region: an approach to estimate carbon isotope rectification, Tellus B, 58, 537–549, 2006.

Chen, J. M., Liu, J., Cihlar, J., and Goulden, M. L.: Daily canopy photosynthesis model through temporal and spatial scaling for remote sensing applications, Ecol. Model., 124, 99–119, 1999.

Chen, J. M., Ju, W., Cihlar, J., Price, D., Liu, J., Chen, W., Pan, J., Black, T. A., and Barr, A.: Spatial distribution of carbon sources and sinks in Canada's forests based on remote sensing, Tellus B, 55, 622–642, 2003.

ACPD
13, 26529–26578, 2013

Chen, J. M., Menges, C. H., and Leblanc, S. G.: Global derivation of the vegetation clumping index from multi-angular satellite data, Remote Sens. Environ., 97, 447–457, 2005.
Chen, J. M., Mo, G., Pisek, J., Liu, J., Deng, F., Ishizawa, M., and Chan, D.: Effects of foliage clumping on the estimation of global terrestrial gross primary productivity, Global Biogeochem. Cy., 26, GB1019, doi:10.1029/2010GB003996, 2012.
Ciais, P., Tans, P. P., Trolier, M., White, J. W. C., and Francey, R. J.:. A large Northern-Hemisphere terrestrial CO_2 sink indicated by the $^{13}C/^{12}C$ ratio of atmospheric CO_2, Science, 269, 1098–1102, 1995a.
Ciais, P., Tans, P. P., White, J. W. C., Trolier, M., Francey, R. J., Berry, J. A., Randall, D. R., Sellers, P. J., Collatz, J. G., and Schimel, D. S.: Partitioning of ocean and land uptake of CO_2 as inferred by $\delta^{13}C$ measurements from the NOAA Climate Monitoring and Diagnostics Laboratory Global Air Sampling Network, J. Geophys. Res., 100, 5051–5070, doi:10.1029/94JD02847, 1995b.
Deng, F. and Chen, J. M.: Recent global CO_2 flux inferred from atmospheric CO_2 observations and its regional analyses, Biogeosciences, 8, 3263–3281, doi:10.5194/bg-8-3263-2011, 2011.
Deng, F., Chen, J. M., Plummer, S., Chen, M., and Pisek, J.: Algorithm for global leaf area index retrieval using satellite imagery, IEEE T. Geosci. Remote, 44, 2219–2229, 2006.
Deng, F., Chen, J. M., Ishizawa, M., Yuen, C.-W., Mo, G., Higuchi, K. A. Z., Chan, D., and Maksyutov, S.: Global monthly CO_2 flux inversion with a focus over North America, Tellus B, 59, 179–190, 2007.
Enting, I. G.: Inverse Problems in Atmospheric Constituents transport, ISBN: 0521812100, Cambridge University Press, Cambridge, UK, 2002.
Enting, I. G., Trudinger, C. M., Francey, R. J., and Granek, H.: Synthesis inversion of atmospheric CO_2 using the GISS tracer transport model, Division of Atmospheric Research technical paper, No. 29, CSIRO Australia, 1993.
Enting, I. G., Trudinger, C. M., and Francey, R. J.: A synthesis inversion of the concentration and $\delta^{13}C$ of atmospheric CO_2, Tellus B, 47, 35–52, 1995.
Farquhar, G. D. and Richards, R. A.: Isotopic composition of plant carbon correlates with water-use efficiency of wheat genotypes, J. Aust. Plant. Physiol., 11, 539–552, 1984.
Farquhar, G. D., von Caemmerer, S., and Berry, J. A.: A biochemical model of photosynthetic CO_2 assimilation in leaves of C3 species, Planta, 149, 78–90, doi:10.1007/BF00386231, 1980.

ACPD
13, 26529–26578, 2013

Farquhar, G. D., Ehleringer, J. R., and Hubick, K. T.: Carbon isotope discrimination and photosynthesis, Ann. Rev. Plant Physiol., 40, 503–537, 1989.

Francey, R. J., Tans, P. P., Allison, C. E., Enting, I. G., White, J. W. C., and Trolier, M.: Changes in oceanic and terrestrial carbon uptake since 1982, Nature, 373, 326–330, 1995.

Francey, R. J., Allison, C. E., Etheridge, D. M., Trudinger, C. M., Enting, I. G., Leuenberger, M., Langenfelds, R. L., Michel, E., and Steele, L. P.: A 1000-year high precision record of $\delta^{13}C$ in atmospheric CO_2, Tellus B, 51, 170–193, 1999.

Fung, I. Y., Field, C. B., Berry, J. A., Thompson, M. V., Randerson, J. T., Malmström, C. M., Vitousek, P. M., James Collatz, G., Sellers, P. J., Randall, D. A., Denning, A. S., and Badeck, F.: Carbon-13 exchanges between the atmosphere and biosphere, Global Biogeochem. Cy., 11, 507–533, 1997.

Garrigues, S., Lacaze, R., Baret, F., Morisette, J. T., Weiss, M., Nickeson, J. E., Fernandes, R., Plummer, S., Shabanov, N. V., Myneni, R. B., Knyazikhin, Y., and Yang, W.: Validation and intercomparison of global Leaf Area Index products derived from remote sensing data, J. Geophys. Res., 113, G02028, doi:10.1029/2007JG000635, 2008.

GLOBALVIEW-CO2C13: Cooperative Atmospheric Data Integration Project – $\delta^{13}C$ of Carbon Dioxide, CD-ROM, NOAA ESRL, Boulder, Colorado, also available at: ftp://ftp.cmdl.noaa.gov/ccg/co2c13/GLOBALVIEW/, Path: ccg/co2c13/GLOBALVIEW, 2009.

Govind, A. and Chen, J. M.: Spatially distributed modeling of the long-term carbon balance of a boreal landscape, Ecol. Model., 222, 2780–2795, doi:10.1016/j.ecolmodel.2011.04.007, 2011.

Gurney, K. R., Law, R. M., Denning, A. S., Rayner, P. J., Baker, D., Bousquet, P., Bruhwiler, L., Chen, Y. H., Ciais, P., Fan, S. M., Fung, I. Y., Manuel Gloor, Martin Heimann, Higuchi,K, John, J., Maki,T, Maksyutov, S., Masarie, K., Peylin, P., Prather, M., Pak, B. C., Randerson, J. T., Sarmiento, J. L., Taguchi, S., Takahashi,T, and Yuen, C. W.: Towards robust regional estimates of CO_2 sources and sinks using atmospheric transport models, Nature, 415, 626–630, 2002.

Gurney, K. R., Gurney, K. R., Law, R. M., Denning, A. S., Rayner, P. J., Baker, D., Bousquet, P., Bruhwiler, L., Chen, Y. H., Ciais, P., Fan, S. M., Fung, I. Y., Gloor, M., Heimann, M., Higuchi, K., John, J., Kowalczyk, E., Maki, T., Maksyutov, S., Peylin, P., Prather, M., Pak, B. C., Sarmiento, J. L., Taguchi, S., Takahashi, T., and Yuen, C. W.: TransCom3 CO_2 inversion intercomparison: 1. Annual mean control results and sensitivity to transport and prior flux information, Tellus B, 55, 555–579, 2003.

ACPD
13, 26529–26578, 2013

Harley, P. C., Loreto, F., Di Marco, G., and Sharkey, T. D.: Theoretical considerations when estimating the mesophyll conductance to CO_2 flux by analysis of the response of photosynthesis to CO_2, Plant Physiol., 98, 1429–1436, 1992.

Houghton, R. A.: Balancing the global carbon budget, Ann. Rev. Earth Planet. Sci., 35, 313–347, 2007.

Ise, T., Litton, C. M., Giardina, C. P., and Ito, A.: Comparison of modeling approaches for carbon partitioning: impact on estimates of global net primary production and equilibrium biomass of woody vegetation from MODIS GPP, J. Geophys. Res., 115, G04025, doi:10.1029/2010JG001326, 2010.

Ju, W. and Chen, J. M.: Distribution of soil carbon stocks in Canada's forests and wetland simulated based on drainage class, topography and remote sensing, Hydrol. Process., 19, 77–94, 2005.

Kalnay, E., Kanamitsu, M., Kistler, R., Collins, W., Deaven, D., Gandin, L., Iredell, M., Saha, S., White, G., Woollen, J., Zhu, Y., Leetmaa, A., Reynolds, B., Chelliah, M., Ebisuzaki, W., Higgins, W., Janowiak, J., Mo, K. C., Ropelewski, C., Wang, J., Jenne, R., and Joseph, D.: The NCEP/NCAR 40-year reanalysis project, B. Am. Meteorol. Soc., 77, 437–471, 1996.

Kanamitsu, M., Ebisuzaki, W., Woollen, J., Yang, S.-K., Hnilo, J. J., Fiorino, M., and Potter G. L.: NCEP-DEO AMIP-II Reanalysis (R-2), B. Am. Meterol. Soc., 83, 1631–1643, 2002.

Keeling, C. D., Bacastow, R. B., Carter, A. F., Piper, S. C., Whorf, T. P., Heimann, M., Mook, W. G., and Roeloffzen, H.: A three-dimensional model of atmospheric CO_2 transport based on observed winds: 1. analysis of observational data, In: Aspects of Climate Variability in the Pacific and Western Americas, edited by: Peterson, D. H., American Geophysical Union, Washington DC, 165–236, 1989a.

Keeling, C. D., Piper, S. C., and Heimann, M.: A three-dimensional model of atmospheric CO_2 transport based on observed winds: 4. mean annual gradients and interannual variations, in: Aspects of Climate Variability in the Pacific and Western Americas, edited by: Peterson, D. H., American Geophysical Union, Washington DC, 305–363, 1989b.

Krol, M. C., Lelieveld, J., Oram, D. E., Sturrock, G. A., Penkett, S. A., Brenninkmeijer, C. A. M., Gros, V., Williams, J., and Scheeren, H. A.: Continuing emissions of methyl chloroform from Europe, Nature, 421, 131–135, 2003.

Krol, M., Houweling, S., Bregman, B., van den Broek, M., Segers, A., van Velthoven, P., Peters, W., Dentener, F., and Bergamaschi, P.: The two-way nested global chemistry-

ACPD
13, 26529–26578, 2013

transport zoom model TM5: algorithm and applications, Atmos. Chem. Phys., 5, 417–432, doi:10.5194/acp-5-417-2005, 2005.

Le Quéré, C., Raupach, M. R., Canadell, J. G., Marland,G, Bopp, L., Ciais, P., Conway, T. J., Doney, S. C., Feely, R., Foster, P., Friedlingstein, P., Gurney, K., Houghton, R. A., House, J. I., Huntingford, C., Levy, P. E., Lomas, M. R., Majkut, J., Metzl, N., Ometto, J. P., Peters, G. P., Prentice, I. C., Randerson, J. T., Running, S. W., Sarmiento, J. L., Schuster, U., Sitch, S., Takahashi, T., Viovy, N., van der Werf, G. R., and Woodward F. I.: Trends in the sources and sinks of carbon dioxide, Nat. Geosci., 2, 831–836, doi:10.1038/ngeo689, 2009.

Liu, J., Chen, J. M., Cihlar, J., and Park, W. M.: A process-based boreal ecosystem productivity simulator using remote sensing inputs, Remote Sens. Environ., 62, 158–175, 1997.

Madec, G., Delecluse, P., Imbard, M., and Lévy, C.: OPA 8.1 ocean general circulation model reference manual, Notes du pôle de modélisation IPSL, 91 pp., available at: http://www.lodyc.jussieu.fr/opa/, 1998.

Marland, G., Boden, T. A., and Andres, R. J.: Global, regional, and national fossil fuel CO_2 emissions, in: Trends: A Compendium of Data on Global Change, Carbon Dioxide Information Analysis Center, Oak Ridge National Laboratory, US Department of Energy, Oak Ridge, Tenn., USA, 2009.

Masarie, K. A. and Tans, P. P.: Extension and integration of atmospheric carbon dioxide data into a globally consistent measurement record, J. Geophys. Res., 100, 11593–11610, 1995.

Michalak, A. M., Hirsch, A., Bruhwiler, L., Gurney, K. R., Peters, W., and Tans, P. P.: Maximum likelihood estimation of covariance parameters for Bayesian atmospheric trace gas surface flux inversions, J. Geophys. Res., 110, D24107, doi:10.1029/2005JD005970, 2005.

Olivier, J. G. J., Van Aardenne, J. A., Dentener, F. J., Pagliari, V., Ganzeveld, L. N., and Peters, J. A. H. W.: Recent trends in global greenhouse gas emissions: regional trends 1970–2000 and spatial distribution of key sources in 2000, Environ. Sci., 2, 81–99, 2005.

Patra, P. K., Maksyutov, S., Ishizawa, M., Nakazawa, T., Takahashi, T., and Ukita, J.: Interannual and decadal changes in the sea-air CO_2 flux from atmospheric CO_2 inverse modeling, Global Biogeochem. Cy., 19, GB4013, doi:10.1029/2004GB002257, 2005.

Peters, W., Miller, J. B., Whitaker, J., Denning, S. A., Hirsch, A., Krol, M., Zupanski, D., Bruhwiler, L., and Tans, P. P.: An ensemble data assimilation system to estimate CO_2 surface fluxes from atmospheric trace gas observations, J. Geophys. Res., 110, D24304, doi:10.1029/2005JD006157, 2005.

ACPD
13, 26529–26578, 2013

Peters, W., Jacobson, W. A. R., Sweeney, C., Andrews, A. E., Conway, T. J., Masarie, K., Miller, J. B., Bruhwiler, L. M. P., Petron, G., Hirsch, A. I., Worthy, D. E. J., Werf, G. R., Randerson, J. T., Wennberg, P. O., Krol, M. C., and Tans, P. P.: An atmospheric perspective on North American carbon dioxide exchange: CarbonTracker, P. Natl. Acad. Sci. USA, 104, 18925–18930, 2007.

Peylin, P., Bousquet, P., Le Quéré, C., Sitch, S., Friedlingstein, P., McKinley, G., Gruber, N., Rayner, P., and Ciais, P.: Multiple constraints on regional CO_2 flux variations over land and oceans, Global Biogeochem. Cy., 19, GB1011, doi:10.1029/2003GB002214, 2005.

Pickett-Heaps, C. A.: Atmospheric CO_2 Inversion Cross-Validation Using Non-Surface CO_2 Data, Ph.D. dissertation, University of Melbourne, Australia, 2007.

Randerson, J. T., Collatz, G. J., Fessenden, J. E., Munoz, A. D., Still, C. J., Berry, J. A., Fung, I. Y., Suits, N., and Denning, A. S.: A possible global covariance between terrestrial gross primary production and ^{13}C discrimination: consequences for the atmospheric ^{13}C budget and its response to ENSO, Global Biogeochem. Cy., 16, 1136, doi:10.1029/2001GB001845, 2002.

Randerson, J. T., van der Werf, G. R., Giglio, L., Collatz, G. J., and Kasibhatla, P. S.: Global Fire Emissions Database, Version 2 (GFEDv2.1), Data set, available at: http://daac.ornl.gov/ from Oak Ridge National Laboratory Distributed Active Archive Center, Oak Ridge, Tennessee, USA, 2007.

Rayner, P. J., Enting, I. G., Francey, R. J., and Langenfelds, R. L.: Reconstructing the recent carbon cycle from atmospheric CO_2, $\delta^{13}C$ and O_2/N_2 observations, Tellus, Ser. B, 51, 213–232, 1999.

Rayner, P. J., Law, R. M., Allison, C. E., Francey, R. J., Trudinger, C. M., and Pickett-Heaps, C.: Interannual variability of the global carbon cycle (1992–2005) inferred by inversion of atmospheric CO_2 and $\delta^{13}CO_2$ measurements, Global Biogeochem. Cy., 22, GB3008, doi:10.1029/2007GB003068, 2008.

Reynolds, R. W and Smith, T. M.: Improved global sea surface temperature analyses using optimum interpolation, J. Climate, 7, 929–948, 1994.

Reynolds, R. W., Rayner, N. A., Smith, T. M., Stokes, D. C., and Wang, W.: An improved in situ and satellite SST analysis for climate, J. Climate, 15, 1609–1625, 2002.

Rödenbeck, C., Houweling, S., Gloor, M., and Heimann, M.: CO_2 flux history 1982–2001 inferred from atmospheric data using a global inversion of atmospheric transport, Atmos. Chem. Phys., 3, 1919–1964, doi:10.5194/acp-3-1919-2003, 2003.

ACPD
13, 26529–26578, 2013

Scholze, M., Ciais, P., and Heimann, M.: Modeling terrestrial ^{13}C cycling: climate, land use and fire, Global Biogeochem. Cy., 22, GB1009, doi:10.1029/2006GB002899, 2008.
Siegenthaler, U. and Oeschger, H.:. Biospheric CO_2 emissions during the past 200 years reconstructed by deconvolution of ice core data, Tellus B, 39, 140–154, 1987.
Sprintsin, M., Chen, J. M., and Czurylowicz, P.: Combining land surface temperature and shortwave infrared reflectance for early detection of mountain pine beetle infestations in western Canada, J. Appl. Remote Sens., 5, 053566, doi:10.1117/1.3662866, 2011.
Suits, N. S., Denning, A. S., Berry, J. A., Still, C. J., Kaduk, J., Miller, J. B., and Baker, I. T.: Simulation of carbon isotope discrimination of the terrestrial biosphere, Global Biogeochem. Cy., 19, GB1017, doi:10.1029/2003GB002141, 2005.
Still, C. J., Berry, J. A., Collatz, G. J., and DeFries, R. S.: Global distribution of C3 and C4 vegetation: carbon cycle implications, Global Biogeochem. Cy., 17, 1006, doi:10.1029/2001GB001807, 2003.
Tans, P. P., Fung, I. Y., and Takahashi, T.: Observational contrains on the global atmospheric CO_2 budget, Science, 247, 1431–1438, 1990.
Tans, P. P., Berry, J. A., and Keeling, R. F.: Oceanic ^{13}C data: A new window on CO_2 uptake by the oceans, Global Biogeochem. Cy., 7, 353–368, 1993.
Tarantola, A.: Inverse Problem Theory, Elsevier, Amsterdam, the Netherlands, 605 pp., 1987.
van der Werf, G. R., Randerson, J. T., Giglio, L., Collatz, G. J., Kasibhatla, P. S., and Arellano Jr., A. F.: Interannual variability in global biomass burning emissions from 1997 to 2004, Atmos. Chem. Phys., 6, 3423–3441, doi:10.5194/acp-6-3423-2006, 2006.
Webb, R. S., Rosenzweig, C. E., and Levine, E. R.: A global data set of soil particle size properties, NASA Tech. Memo., TM-4286, 40 pp., 1991.
Zhang, F., Chen, J. M., Chen, J., Gough, C. M., Martin, T. A., and Dragoni, D.: Evaluating spatial and temporal patterns of MODIS GPP over the conterminous US against flux measurements and a process model, Remote Sens. Environ., 124, 717–729, 2012.

ACPD
13, 26529–26578, 2013

Table 1. Biophysical parameters are assigned by plant functional types in BEPS. References for the chosen values of these parameters are found in Chen et al. (2012).

Parameters*	Broadleaf Evergreen	Broadleaf Deciduous	Evergreen Conifers	Deciduous Conifers	Shrub	C4 Plants	Others
V_{cmax} $\mu mol\,m^{-2}\,s^{-1}$ (at 25 °C)	29.0 ± 7.7	57.7 ± 21.2	62.5 ± 24.7	39.1 ± 11.7	57.9 ± 19.6	100.7 ± 36.6	90.0 ± 89.5
J_{max} $\mu mol\,m^{-2}\,s^{-1}$	55.1	123.7	135.2	79.2	124.1	193.1	200.0
N $g\,m^{-2}$	2.17 ± 0.8	1.74 ± 0.71	3.10 ± 1.35	1.81 ± 0.64	1.86 ± 0.84	1.62 ± 0.61	1.69 ± 0.69
χ_n $m^2\,g^{-1}$	0.48	0.59	0.33	0.56	0.57	0.62	0.60
Slope (m)	8	8	8	8	8	4	8
Intercept (b), $mol\,m^{-2}\,s^{-1}$	0.0011	0.0011	0.0011	0.0011	0.0011	0.0011	0.0011
LAI	4.07 ± 2.02	3.14 ± 1.99	3.05 ± 1.62	2.42 ± 1.45	1.49 ± 1.06	1.55 ± 1.22	1.64 ± 1.15
Clumping Index	0.66 ± 0.045	0.70 ± 0.047	0.74 ± 0.057	0.78 ± 0.051	0.75 ± 0.059	0.75 ± 0.050	0.76 ± 0.059
Canopy height (m)	23	23	20	20	4	4	4

* Where V_{cmax} is the leaf maximum carboxylation rate at 25 °C, J_{max} is the maximum electron transport rate, N is the leaf nitrogen content, χ_n is the slope of V_{cmax} variation with N, and m and b are the slope and intercept in the Ball–Berry equation. The peak growing season LAI and clumping index are given as the mean and standard deviation for each plant functional type.

ACPD
13, 26529–26578, 2013

Table 2. Global average ages of soil carbon pools computed by BEPS with consideration of the influences of temperature and soil moisture on the decomposition rates of these pools.

Soil carbon pool i	Name	Global Average Age τ_i (yr)
1	Surface structural leaf litter	2.3
2	Surface metabolic leaf litter	0.9
3	Soil structural litter	1.8
4	Soil metabolic litter	0.6
5	Woody litter	13.4
6	Surface microbe	2.2
7	Soil microbe	14.0
8	Slow carbon	22.0
9	Passive carbon	686.7

ACPD
13, 26529–26578, 2013

Table 3. Inverted fluxes ($Pg\,C\,yr^{-1}$), averaged for 2002–2004, for land (1–39) and ocean (40–50) regions with ($CO_2 + {}^{13}CO_2$) and without (CO_2 only) ^{13}C constraint using the $^{13}CO_2/CO_2$ flux ratio. The negative sign denotes the flux from the atmosphere to the surface (sink). Various treatments are made to this ratio represented by the following cases: Case I: variable ratios for land and ocean regions with full consideration of the regional differences in discrimination and disequilibrium; Case II: variable ratios for ocean regions, but the ratio for land is constant (0.010934). Case III: ratios for both ocean and land are constants at 0.011125 and 0.010934, respectively.

Region	Prior flux	Inverted flux			
		CO_2 only	$CO_2+{}^{13}CO_2$		
			Case 1	Case 2	Case 3
1	−0.000153 ± 0.000487	−0.000028 ± 0.000000	−0.000022 ± 0.000000	−0.000022 ± 0.000000	−0.000022 ± 0.000000
2	0.018018 ± 0.042481	0.027440 ± 0.027946	0.032599 ± 0.026931	0.032116 ± 0.026926	0.032116 ± 0.026926
3	0.004334 ± 0.024737	−0.008985 ± 0.023581	−0.012118 ± 0.023553	−0.012274 ± 0.023553	−0.012275 ± 0.023553
4	−0.005229 ± 0.016981	−0.003204 ± 0.016862	−0.001686 ± 0.016862	−0.001789 ± 0.016862	−0.001784 ± 0.016862
5	−0.003653 ± 0.019410	−0.005009 ± 0.019305	−0.003429 ± 0.019279	−0.003428 ± 0.019279	−0.003426 ± 0.019279
6	0.005874 ± 0.021384	−0.004716 ± 0.021323	−0.005225 ± 0.021307	−0.005224 ± 0.021307	−0.005225 ± 0.021307
7	0.006446 ± 0.029070	−0.006835 ± 0.028850	−0.004468 ± 0.028815	−0.004489 ± 0.028815	−0.004484 ± 0.028815
8	−0.007091 ± 0.025564	−0.008189 ± 0.025462	−0.007379 ± 0.025462	−0.007484 ± 0.025462	−0.007480 ± 0.025462
9	0.003498 ± 0.058216	−0.033042 ± 0.052225	−0.043749 ± 0.052164	−0.043586 ± 0.052164	−0.043648 ± 0.052164
10	−0.001631 ± 0.045533	−0.024145 ± 0.044627	−0.026275 ± 0.044594	−0.025807 ± 0.044594	−0.025826 ± 0.044594
11	−0.007039 ± 0.026418	−0.007550 ± 0.025590	−0.007538 ± 0.025590	−0.007596 ± 0.025590	−0.007596 ± 0.025590
12	−0.012161 ± 0.034406	−0.016400 ± 0.034078	−0.015746 ± 0.034044	−0.015871 ± 0.034044	−0.015872 ± 0.034044
13	−0.012221 ± 0.035139	−0.024263 ± 0.034539	−0.026456 ± 0.034529	−0.026157 ± 0.034529	−0.026164 ± 0.034529
14	−0.018174 ± 0.041373	−0.020990 ± 0.040615	−0.019936 ± 0.040550	−0.019955 ± 0.040550	−0.019962 ± 0.040550
15	−0.005881 ± 0.060536	−0.031152 ± 0.051544	−0.033120 ± 0.051499	−0.033016 ± 0.051499	−0.033025 ± 0.051499
16	0.002570 ± 0.078706	−0.080756 ± 0.074903	−0.079722 ± 0.074671	−0.079103 ± 0.074671	−0.079142 ± 0.074671
17	−0.010252 ± 0.047679	−0.017131 ± 0.045077	−0.010299 ± 0.044925	−0.010788 ± 0.044922	−0.010807 ± 0.044922
18	0.027453 ± 0.035105	−0.032009 ± 0.033336	−0.033770 ± 0.033160	−0.033406 ± 0.033160	−0.033454 ± 0.033160
19	−0.004790 ± 0.020525	−0.005701 ± 0.020396	−0.006478 ± 0.020380	−0.006360 ± 0.020380	−0.006364 ± 0.020380
20	−0.045119 ± 0.062417	−0.036769 ± 0.059827	−0.045235 ± 0.059713	−0.045857 ± 0.059713	−0.045904 ± 0.059713
21	−0.025155 ± 0.068549	−0.073483 ± 0.062218	−0.078155 ± 0.061554	−0.078409 ± 0.061554	−0.078467 ± 0.061554
22	−0.037121 ± 0.076034	−0.097356 ± 0.061609	−0.103218 ± 0.061526	−0.102814 ± 0.061526	−0.102932 ± 0.061526
23	0.003098 ± 0.008893	0.003917 ± 0.008888	0.003642 ± 0.008813	0.003662 ± 0.008813	0.003657 ± 0.008813
24	0.004883 ± 0.000613	0.007617 ± 0.000000	0.007615 ± 0.000000	0.007615 ± 0.000000	0.007615 ± 0.000000
25	−0.008507 ± 0.014522	−0.001135 ± 0.014248	−0.001655 ± 0.014236	−0.001654 ± 0.014236	−0.001658 ± 0.014236

ACPD
13, 26529–26578, 2013

Table 3. Continued.

Region	Prior flux	Inverted flux			
		CO_2 only	$CO_2+{}^{13}CO_2$		
			Case 1	Case 2	Case 3
26	−0.079285 ± 0.074656	−0.045212 ± 0.067754	−0.051920 ± 0.067675	−0.052070 ± 0.067675	−0.052146 ± 0.067675
27	−0.069061 ± 0.083322	−0.061862 ± 0.079922	−0.066313 ± 0.079759	−0.064105 ± 0.079759	−0.064347 ± 0.079759
28	−0.000161 ± 0.076153	−0.035562 ± 0.067408	−0.031827 ± 0.065914	−0.030740 ± 0.065904	−0.031028 ± 0.065904
29	−0.026854 ± 0.040809	−0.012564 ± 0.040133	−0.015220 ± 0.040062	−0.015382 ± 0.040062	−0.015375 ± 0.040062
30	−0.023115 ± 0.045813	−0.015675 ± 0.044989	−0.021600 ± 0.044918	−0.021156 ± 0.044918	−0.021143 ± 0.044918
31	−0.834170 ± 0.724645	0.435965 ± 0.459981	0.042909 ± 0.452773	0.140193 ± 0.452917	0.152219 ± 0.452919
32	−0.182482 ± 0.470911	0.009433 ± 0.277009	−0.049749 ± 0.269118	−0.065403 ± 0.269097	−0.071693 ± 0.269090
33	−0.282139 ± 0.506122	−0.237814 ± 0.271470	−0.176503 ± 0.256905	−0.225278 ± 0.257025	−0.227676 ± 0.257024
34	−0.349811 ± 0.678251	−0.797565 ± 0.257852	−0.849710 ± 0.253974	−0.855741 ± 0.253973	−0.858134 ± 0.253971
35	−0.109829 ± 0.916156	−0.973941 ± 0.244627	−0.893067 ± 0.238453	−0.871698 ± 0.238412	−0.872909 ± 0.238405
36	0.106515 ± 0.553002	−0.467640 ± 0.236845	−0.749632 ± 0.224053	−0.777367 ± 0.224067	−0.778721 ± 0.224064
37	−0.372883 ± 0.379844	−0.489911 ± 0.221711	−0.110411 ± 0.195401	−0.096640 ± 0.195305	−0.097762 ± 0.195304
38	−0.044075 ± 0.092377	0.081029 ± 0.081608	0.081114 ± 0.081036	0.076480 ± 0.081040	0.076203 ± 0.081040
39	−0.215118 ± 0.734214	−0.285777 ± 0.206398	−0.290699 ± 0.197903	−0.280365 ± 0.197834	−0.280830 ± 0.197834
40	−0.809641 ± 0.396123	−0.340903 ± 0.187581	−0.283630 ± 0.179255	−0.289124 ± 0.179262	−0.285265 ± 0.179239
41	−0.085911 ± 0.036900	−0.088658 ± 0.036240	−0.085637 ± 0.036185	−0.086335 ± 0.036185	−0.086385 ± 0.036185
42	0.641049 ± 0.286609	0.693543 ± 0.183068	0.855177 ± 0.179813	0.824769 ± 0.179937	0.818156 ± 0.179976
43	−0.606403 ± 0.292319	−0.408198 ± 0.167455	−0.422187 ± 0.159300	−0.426330 ± 0.159302	−0.423930 ± 0.159274
44	−0.231750 ± 0.099693	−0.273591 ± 0.064331	−0.266650 ± 0.062621	−0.271678 ± 0.062623	−0.271868 ± 0.062629
45	−0.235457 ± 0.149046	−0.293825 ± 0.124730	−0.259099 ± 0.123254	−0.259444 ± 0.123254	−0.257030 ± 0.123250
46	0.028464 ± 0.027225	0.025647 ± 0.026938	0.026497 ± 0.026913	0.026477 ± 0.026913	0.026377 ± 0.026913
47	−0.245375 ± 0.136151	−0.236662 ± 0.120807	−0.183432 ± 0.119999	−0.182979 ± 0.119999	−0.182473 ± 0.119999
48	−0.178222 ± 0.164797	0.035508 ± 0.054990	0.045896 ± 0.053570	0.046275 ± 0.053570	0.045825 ± 0.053570
49	−0.051310 ± 0.024085	−0.037624 ± 0.023965	−0.036312 ± 0.023930	−0.036403 ± 0.023930	−0.036489 ± 0.023930
50	−0.351851 ± 0.210732	−0.557065 ± 0.141205	−0.510856 ± 0.139233	−0.513037 ± 0.139236	−0.510200 ± 0.139228
land	−2.610468 ± 2.073247	−3.396969 ± 0.835866	−3.704451 ± 0.808841	−3.660968 ± 0.808903	−3.665471 ± 0.808898
ocean	−2.126406 ± 0.670409	−1.481826 ± 0.395737	−1.120233 ± 0.384988	−1.167809 ± 0.385052	−1.163282 ± 0.385044

ACPD
13, 26529–26578, 2013

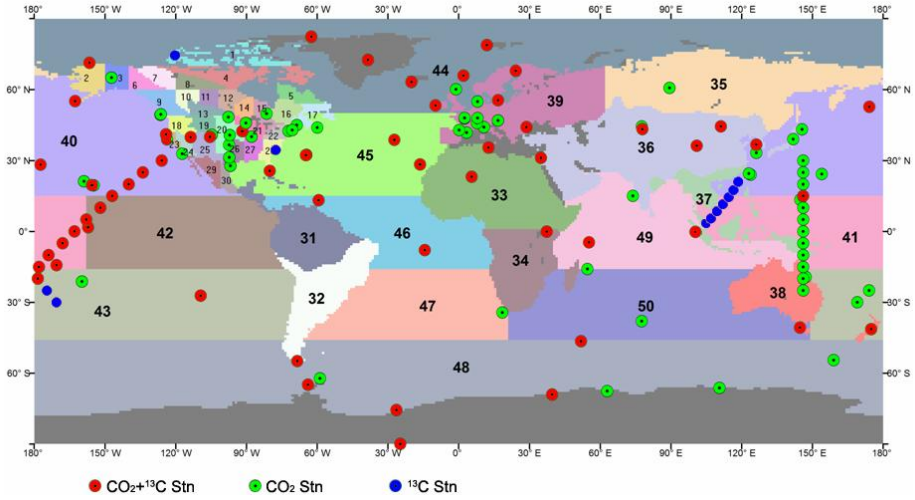

Fig. 1. A global nested inversion system with a focus in North America, in which oceans are divided into 11 regions and land areas are divided into 9 large and 30 small regions outside and within North America, respectively. Also shown are CO_2 and $^{13}CO_2$ observation stations included in the GlobalView database and used in this study.

ACPD
13, 26529–26578, 2013

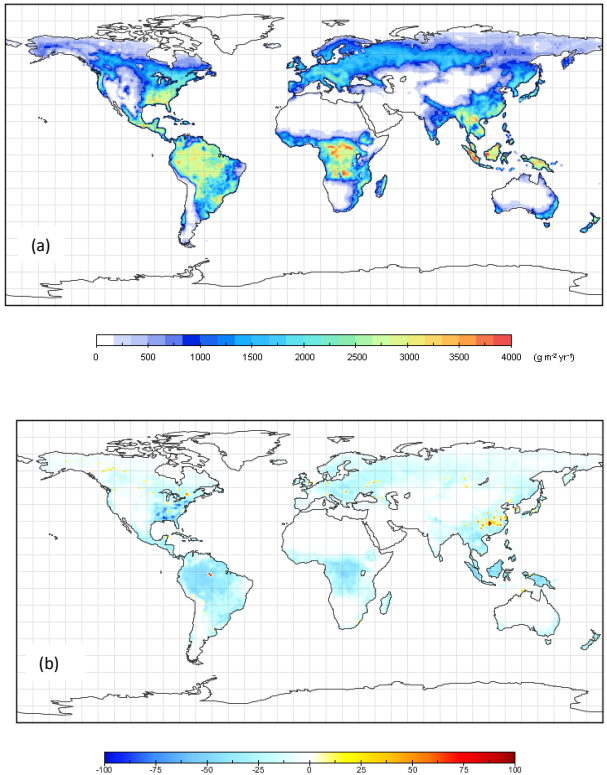

Fig. 2. (a) gross primary productivity (GPP) distribution in 2003 computed using remote sensing LAI and land cover maps and climate and soil data, and **(b)** net ecosystem productivity (NEP) distribution in 2003. Both are calculated using the BEPS model. Annual NEP maps from 2000 to 2004 are used to as the prior flux in the inversions. This GPP map is used to distribute the flux uncertainty among the 39 land regions.

ACPD
13, 26529–26578, 2013

Atmospheric inversion of the surface CO_2 flux with $^{13}CO_2$ constraint

J. M. Chen et al.

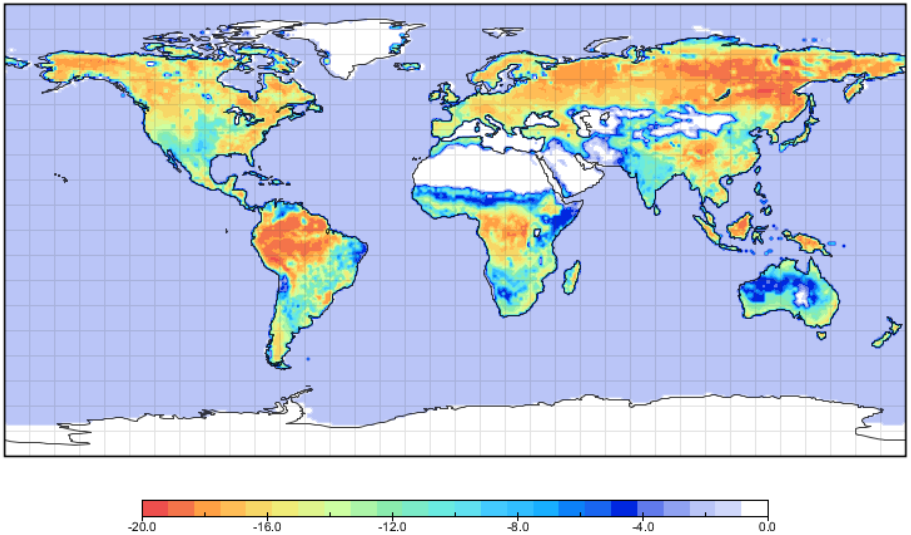

Fig. 3. The annual mean of the total photosynthetic ^{13}C discrimination (Δ in Eq. 7) in 2003.

ACPD
13, 26529–26578, 2013

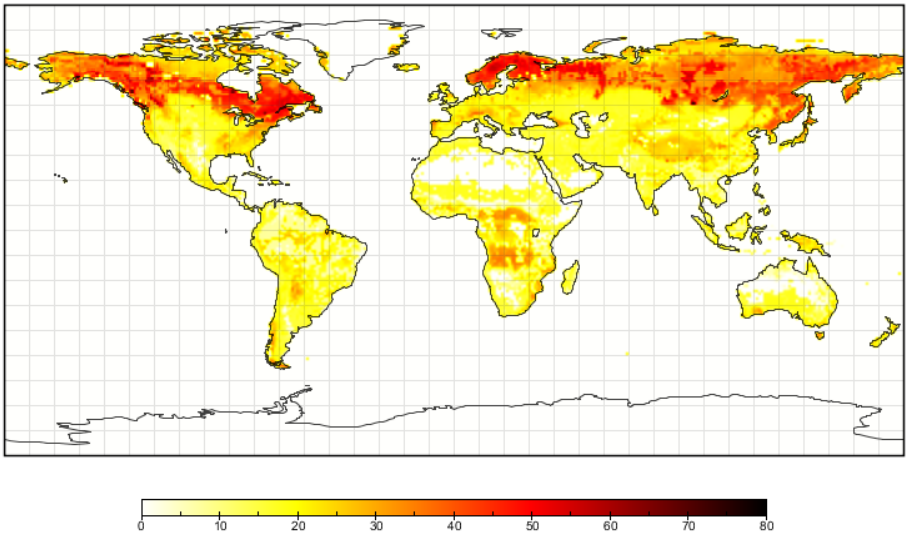

Fig. 4. Global distribution of the flux-weighted mean age of soil carbon pools (Eq. 8).

ACPD
13, 26529–26578, 2013

Atmospheric inversion of the surface CO_2 flux with $^{13}CO_2$ constraint

J. M. Chen et al.

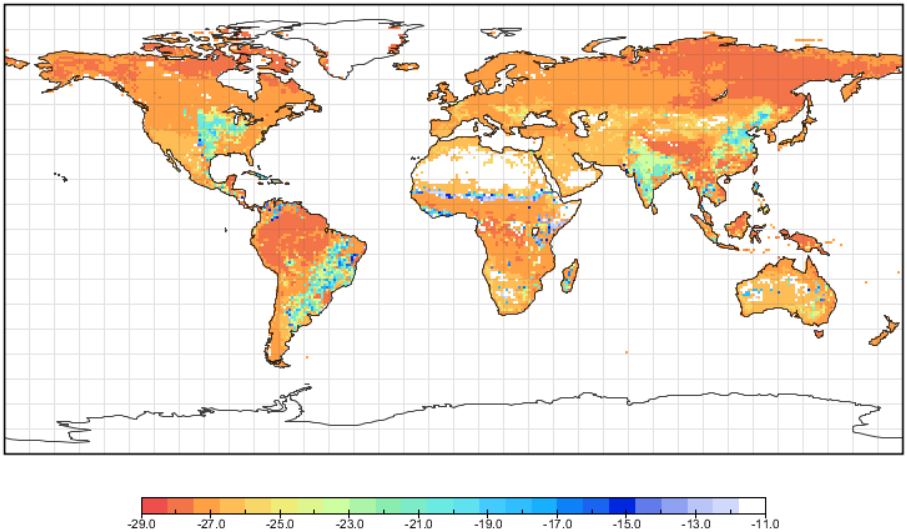

Fig. 5. Global δ^{13}C distribution over land (annual flux-weighted average in 2003).

ACPD
13, 26529–26578, 2013

Atmospheric inversion of the surface CO_2 flux with $^{13}CO_2$ constraint

J. M. Chen et al.

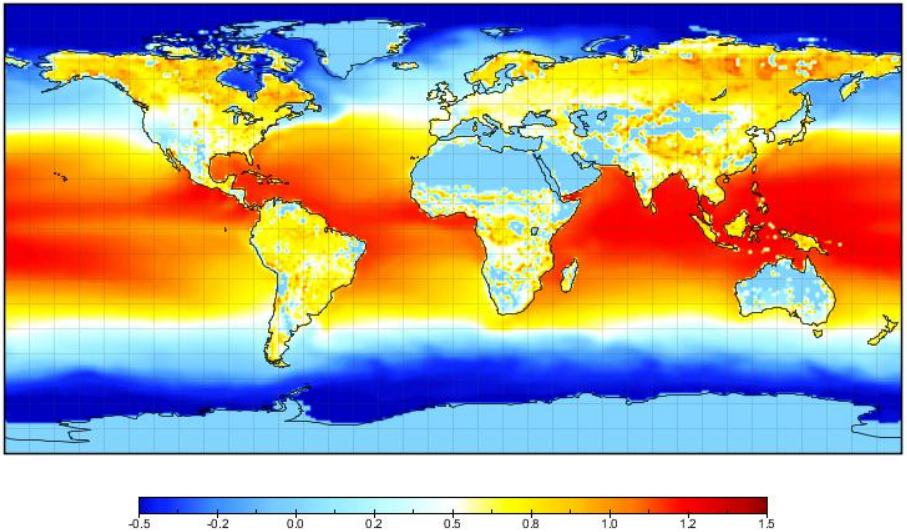

Fig. 6. Disequilibria between ^{13}C fluxes to and from the land or ocean surface in 2000. At the land surface, the disequilibrium is the difference between photosynthetic and respiratory discriminations against ^{13}C, and at the ocean surface, it is the difference in ^{13}C discrimination between the one-way diffusive downward and upward fluxes.

ACPD
13, 26529–26578, 2013

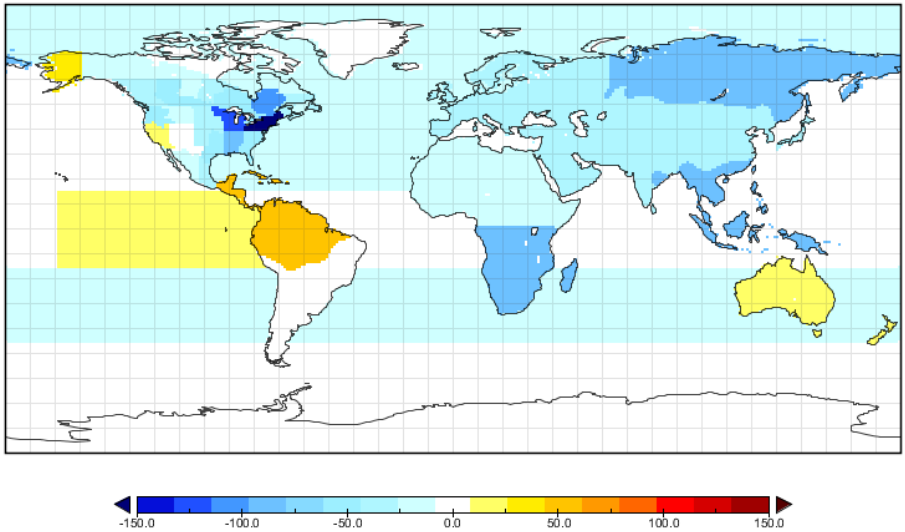

Fig. 7. Global distribution of inverted CO_2 flux using CO_2 data only (2002–2004 average).

ACPD
13, 26529–26578, 2013

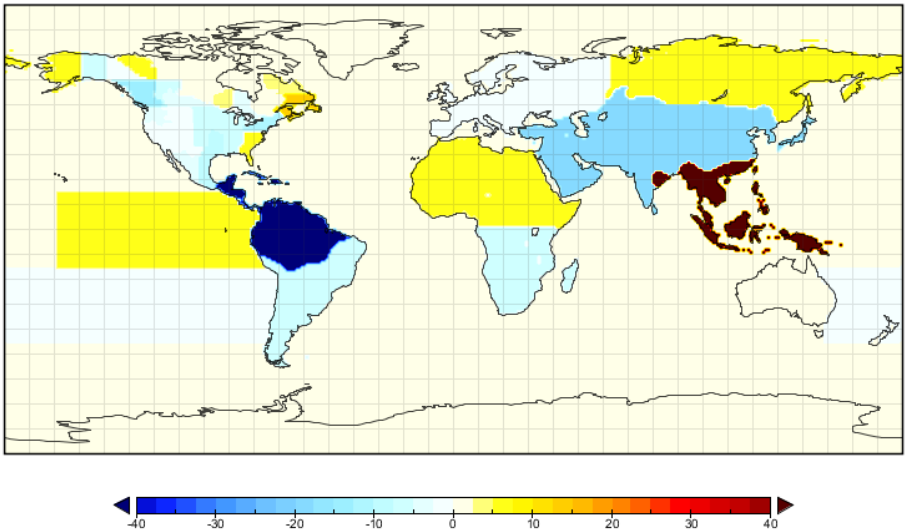

Fig. 8. Difference of inverted CO_2 flux between using $CO_2 + {}^{13}CO_2$ data and using CO_2 data only ($g\,C\,m^{-2}yr^{-1}$, 2002–2004 average).

ACPD
13, 26529–26578, 2013

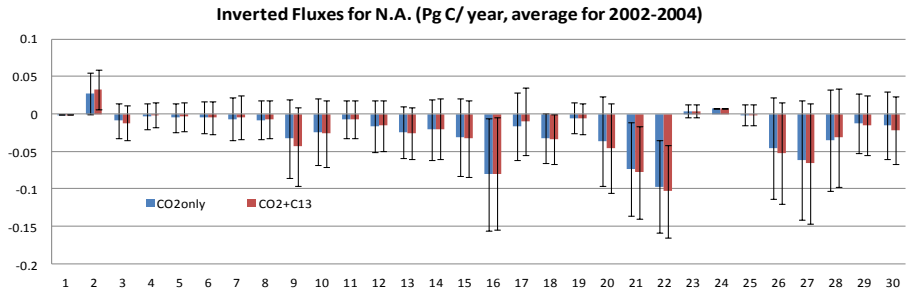

Fig. 9. Comparison between inversion results with and without $^{13}CO_2$ constraint for 30 regions in North America.

ACPD
13, 26529–26578, 2013

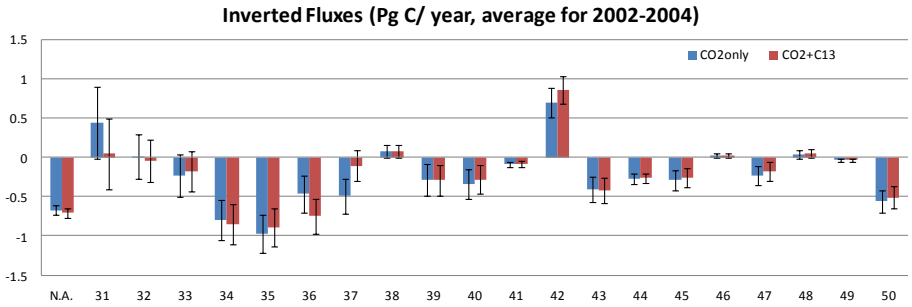

Fig. 10. Comparison between inversion results with and without $^{13}CO_2$ constraint for 21 regions of the globe for the periods of 2002–2004.

ACPD
13, 26529–26578, 2013

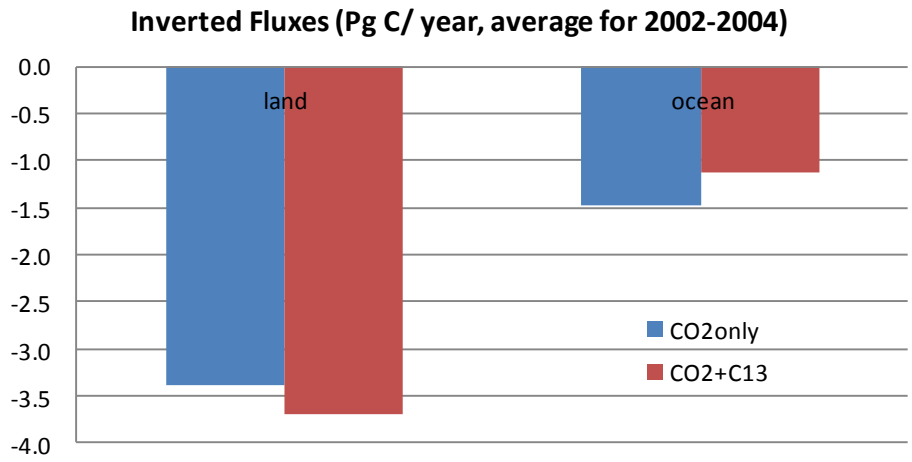

Fig. 11. Summary of inversion results with and without $^{13}CO_2$ constraint for ocean and land for the period of 2002–2004.

ACPD
13, 26529–26578, 2013

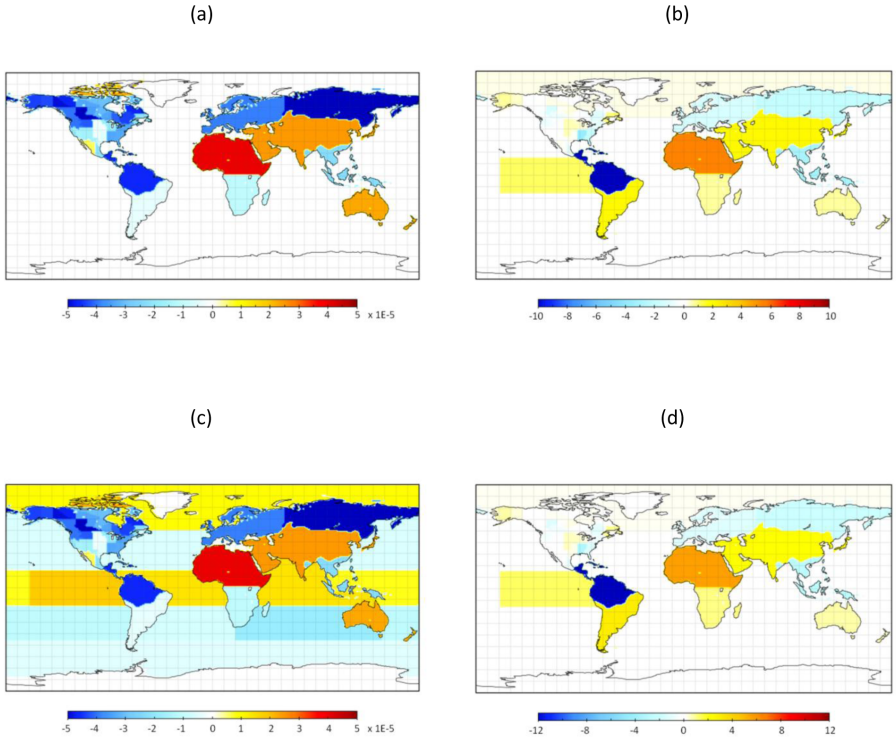

Fig. 12. Differences in the $^{13}CO_2/CO_2$ flux ratio and the inverted CO_2 flux ($g\,C\,m^{-2}yr^{-1}$) between Case I and Case II (plates **a** and **b**), and between Case I and Case III (**c** and **d**). See Sect. 2.1.3 for the description of these cases.

ACPD
13, 26529–26578, 2013